Carbon 261 (2027) 122113

Contents lists available at ScienceDirect

Carbon

journal homepage: www.elsevier.com/locate/carbon

Confined pyrolysis synthesis of 3D hierarchical Ni-NC scaffolds as monolithic flow-through electrodes with high-efficiency electrocatalysis for broad-spectrum antibiotic detoxification

Yingjie Ruan [a,b], Jiangnan Huang [a,*], Ruping Yan [c], Xingan Cheng [a], Hao-Fan Wang [b], Hongjuan Wang [b], Peng Zhao [c,**], Hao Yu [b], Yonghai Cao [b,***]

[a] College of Chemistry and Chemical Engineering, Zhongkai University of Agriculture and Engineering, Guangzhou, 510550, China
[b] School of Chemistry and Chemical Engineering, Guangdong Provincial KeyLab of Green Chemical Product Technology, South China University of Technology, Guangzhou, 510641, China
[c] NMPA Key Laboratory for Research and Evaluation of Drug Metabolism, Guangdong Provincial Key Laboratory of New Drug Screening, School of Pharmaceutical Sciences, Southern Medical University, Guangzhou, 510515, China

ARTICLE INFO

Keywords:
Ni-NC
Electrocatalytic oxidation
Tetracycline degradation
Hydroxyl radical
Active chlorine species

ABSTRACT

To overcome the mass transfer limitations and catalyst loss issues in conventional electrocatalytic advanced oxidation processes, a three-dimension (3D) carbon-supported nickel with nitrogen co-doped (Ni-NC) monolith electrode containing a hierarchical pore structure was constructed on a nickel foam via a confined pyrolysis process. When applied in a convection-enhanced flow-through reactor, the system achieved a single-pass tetracycline (TC) removal efficiency of 95.82% with a chemical oxygen demand (COD) mineralization of 64.93% and a specific energy consumption of 38.27 kWh kg^{-1} COD. Acid etching and Arrhenius kinetic analyses identified interfacial Ni-N_x coordination and high-valence Ni^{3+} as the active centers, which decreased the apparent activation energy (E_a) of the oxidation process (28.9 kJ mol^{-1}). Mechanistic investigations indicated that the anode triggered the chlorine evolution reaction in high-salinity environments, generating a reactive network dominated by free available chlorine (FAC) and supplemented by •OH to drive the ring-opening and mineralization of the substrates. The electrode maintained the performance and structural integrity over 8 consecutive cycles and a 24-h continuous operation. In addition, the system was evaluated against nine representative antibiotics and maintained effective removal performance. Biological toxicity tests further suggested that the treated effluents exhibited reduced biological toxicity.

1. Introduction

The widespread use of antibiotics and their persistent occurrence in aquatic environments have led to growing environmental concerns [1]. Among them, tetracyclines (TCs) are extensively used in medical treatment, animal husbandry, and aquaculture due to their broad-spectrum antibacterial activity and relatively low cost [2,3]. However, their high persistence and potential to induce antibiotic resistance capability have become a growing issue [1,4]. Critically, many industrial wastewaters, particularly those from antibiotic production, are characterized by high salinity (a total salt content exceeding 1 wt%), which poses a significant challenge for conventional biological treatments [5,6].

Recently, electrochemical advanced oxidation processes (EAOPs) have been increasingly recognized as pivotal technologies for modular, adaptive, and decentralized water treatment paradigms [7,8]. As highlighted in recent comprehensive reviews, advancing EAOPs from conventional batch cells toward continuous flow-based configurations, coupled with the rational design of robust electrocatalytic materials, is imperative to overcome mass-transfer bottlenecks and enhance practical energy efficiency [9]. Also, the process could operate under mild conditions and generate reactive oxygen species *in situ* without the addition of external chemicals [10]. These features make EAOPs attractive for the deep mineralization of organic pollutants. However, their practical performance is often limited by the mismatch between reaction kinetics

* Corresponding author.
** Corresponding author.
*** Corresponding author.
E-mail addresses: huangjiangnan@zhku.edu.cn (J. Huang), smuzp@smu.edu.cn (P. Zhao), meyhcao@scut.edu.cn (Y. Cao).

https://doi.org/10.1016/j.carbon.2026.122113
Received 4 July 2026; Received in revised form 3 September 2026; Accepted 14 September 2026
Available online 16 September 2026
0008-6223/© 2026 Elsevier Ltd. All rights are reserved, including those for text and data mining, AI training, and similar technologies.

and mass transfer. In conventional electrocatalytic systems, such as flow-by or batch reactors [11], the electrolyte mainly flows along a longitudinal axis of the electrode. As a result, mass transport is restricted by the relatively thick Nernst diffusion layer [12,13], and the liquid-phase mass transfer coefficient (k_m) typically remains in the range of 10^{-6}-10^{-5} m s^{-1} [14]. Under such conditions, the degradation efficiency is usually low (<20%), while the energy consumption remains high (>150 kWh m^{-3}) [15,16]. Flow-through configurations provide an alternative by introducing a convection-dominated transport mode, which can significantly enhance mass transfer [14]. For example, Ti_4O_7-based reactive electrochemical membranes have been reported to increase k_m to above 10^{-4} m s^{-1}, enabling efficient pollutant removal within short residence times [17]. Similar improvements have also been observed in porous carbon electrode systems, including graphene aerogels, mesoporous carbon materials and carbon felt [18–21], where three-dimensional three-dimension (3D) interconnected channels facilitate mass transport and improve the accessibility of active sites.

In recent years, atomically dispersed metal-nitrogen-carbon (M-N-C) materials have attracted increasing attention due to their high intrinsic activity and efficient utilization of metal sites [22–26]. For Ni-based systems, the coordination between metal centers and nitrogen atoms can regulate the local electronic structure, which may further influence the adsorption and transformation of reactants and intermediates on the electrode surface [23,27–31]. Especially, for the high salinity solution containing chlorine ions, Ni-N-C catalysts have been reported to exhibit higher activity compared with other transition metal systems such as Fe and Co. This behavior is often attributed to the regulation of competing chlorine evolution (CER) and oxygen evolution reactions (OER). In particular, the local coordination environment of Ni sites may suppress OER while promoting the formation of reactive chlorine species (RCS) [32], which benefiting the treatment of organic pollutants in a solution with high salinity. Furthermore, M-N-C-based materials exhibit excellent compatibility with flow-through systems. Firstly, atomic-level dispersion maximizes the effective surface area. Constructing high-density Ni-N_x sites on three-dimensional macroporous carbon substrates (such as nickel foam-derived carbon or carbon cloth) can provide a high density of active sites [33]. This ensures a sufficient collision probability between pollutant molecules and active centers under high-flux flow-through conditions [34]. Secondly, the covalent bonding of Ni-N endows the electrode with excellent chemical stability [35], effectively resolving the issues of active center loss and passivation commonly observed in traditional coated electrodes during long-term electrolysis. Additionally, the synergy effect between the electrical conductivity of the carbon substrate and the Ni active centers guarantees an extremely high heterogeneous electron transfer rate [36], which is crucial for maintaining low-energy-consumption operation under high throughput. In the treatment of high-salinity wastewater, a single-atom Ni-modified porous carbon membrane as a flow anode could possess the specific catalytic activity for Cl^- oxidation, enabling the *in-situ* generation of high-flux RCS [32]. When treating TC wastewater, this system achieved a degradation efficiency of over 98% within 10 min [37]. However, in flow-through electrocatalytic oxidation systems, a critical question remains urgently to be addressed: how to achieve the synergy between high-throughput convective mass transfer and the efficient generation of specific reactive species (such as RCS/•OH) through the effective regulation of Ni-N-C active sites on molded carbon substrates, thereby balancing mass transfer and activity for antibiotic degradation under high-salt conditions?

Herein, this work proposes a novel strategy for advanced wastewater remediation. By employing a confined pyrolysis approach, a binder-free, self-supporting 3D hierarchical Ni-NC carbon monolith was successfully fabricated. This macroscopic architectural design bridges the critical gap between atomic-level active site engineering and macroscopic electrode stability. More importantly, this study quantitatively decouples the enhancement of hydrodynamic mass transfer from the reduction of intrinsic kinetic barriers. While the flow-through configuration obliterates the sluggish concentration polarization, the specific electron-withdrawing Ni-N_x configurations within the carbon lattice fundamentally slash the apparent activation energy of the oxidation process from 55.1 to 28.9 kJ/mol. Furthermore, by exploiting the unique dynamic interconversion between reactive chlorine species and hydroxyl radicals in a hypersaline matrix, a synergistic catch-and-destroy pathway was established. This allows for targeted ring-opening and deep mineralization of complex antibiotics with exceptional energy efficiency. Ultimately, this work provides profound mechanistic insights and a scalable engineering blueprint for utilizing macroscopic functionalized carbon monoliths in high-throughput electrocatalytic applications.

2. Experimental section

2.1. Synthesis of Ni-NC

Ni-NC was prepared through a one-pot confined pyrolysis approach. NH_4Cl (50 g), melamine (15 g), and a piece of nickel foam (NF, 100 × 50 × 0.3 mm, ~1 g) were placed in a crucible (100 × 50 × 35 mm) in a layered configuration, with NH_4Cl at the bottom and the nickel foam positioned on top. A crucible plate (99 × 49 × 16 mm, ~295 g) was then used to cover the system, forming a confined environment during thermal treatment. The assembly was heated in a tube furnace to 550°C at a rate of 10°C min^{-1} and held for 0.5 h, followed by further heating to 900°C at 5°C min^{-1} with a dwelling time of 3 h, and the entire process was maintained under a low argon atmosphere (10 mL min^{-1}).

After the thermal process, the sample was allowed to cool naturally to room temperature.

To balance the mechanical integrity of the monolithic catalyst with the geometric constraints of the confined space, the mass ratio of melamine to nickel foam was varied (40-60) to obtain a series of Ni-NC materials. The resulting materials were denoted as Ni-NC_x, where x represents the mass ratio of melamine to nickel foam. To prepare the Ni-NC-Acid, the corresponding sample was stirred in 6 mol L^{-1} HCl at room temperature for 12 h, followed by thorough washing with deionized water and drying in an oven overnight.

2.2. Electrocatalytic degradation of TC

TC was selected as a model pollutant to evaluate the electrocatalytic degradation performance in a custom-designed two-electrode flow-through reactor operated in a strict single-pass continuous mode. Typically, the feed solution consisted of 80 mg L^{-1} TC with 2 wt NaCl as the supporting electrolyte. The solution was continuously delivered from a feed reservoir into the reactor using a peristaltic pump at a flow rate of 1 mL min^{-1}. The reaction was initiated immediately by applying a constant current across the reactor. To ensure a genuine single-pass evaluation, the treated effluent was completely discharged without any recirculation. Liquid samples were collected at the outlet at predetermined reaction intervals, filtered through a 0.22 μm organic filter membrane, and analyzed for TC concentration using high-performance liquid chromatography (HPLC). The retention time of TC in the HPLC analysis was 17.3 min, and the TC concentration in the samples was calculated using an external standard method by using COD and TOC analysis (Fig. S1–S3). The TC removal efficiency (X), the chemical oxygen demand (COD) removal percentage (X_{COD}), specific energy consumption (E_{COD}), and average current efficiency (ACE) were calculated using the following equations (Eqs. (1)–(4)):

$$X = \frac{C_0 - C_t}{C_0} \times 100\% \quad (1)$$

$$X_{COD} = \frac{COD_0 - COD_t}{COD_0} \times 100\% \quad (2)$$

$$ACE = \frac{COD_0 - COD_t}{8It} FV \times 100\% \quad (3)$$

$$E_{COD}(KWh/kg\ COD) = \frac{1000\ UIt}{(COD_0 - COD_t)\ V} \quad (4)$$

Where C_0 (mg L^{-1}) and C_t (mg L^{-1}) represent the TC concentrations at the initial time and time t, respectively. COD_0 and COD_t represent the chemical oxygen demand values (mg L^{-1}) of the initial solution and the outlet solution at time t, respectively. F is the Faraday constant (96,485 C mol^{-1}), I is the applied current (A), t is the sampling time (h), V is the volume of the treated solution (L), and U represents the average cell voltage (V) during the sampling period.

The COD of the samples was determined using the standard potassium dichromate method. To strictly eliminate the oxidative interference induced by the high background chloride concentration (20 g/L NaCl), the effluent samples were diluted and excessively masked with $HgSO_4$ prior to digestion at 150°C for 2 h, ensuring the accuracy of the mineralization evaluation.

The electrocatalytic reaction rate (R_E) was evaluated under an applied current of 2 mA, with the flow rate fixed at 10 mL min^{-1}, Effluent samples were collected at the reactor outlet after 90 and 120 min. The kinetic parameters were subsequently derived based on the following equations (Eqs. (5)–(8)):

$$R = \frac{\Delta c}{\Delta t} \quad (5)$$

$$R_E = R_0 - R_0^{'} = k_E c_A^n \quad (6)$$

$$ln\ k_E = \frac{-E_a}{RT} + lnA \quad (7)$$

$$ln\ R = ln\ k + nln\ c_A \quad (8)$$

Here, R_E represents the electrocatalytically driven reaction rate, defined as the difference between the overall TC removal rate under an applied electric field (R_0) and the adsorption rate in the absence of an electric field ($R_0^{'}$) (mmol L^{-1} s^{-1}). Δc denotes the concentration difference between the influent and effluent TC solutions (mg L^{-1}), and Δt corresponds to the residence time of TC within the catalyst channels (s). k_E is the apparent reaction rate constant (mol^{1-n} L^{n-1} s^{-1}), n is the order of reaction, E_a is the apparent activation energy (kJ mol^{-1}), R is the universal gas constant (8.314 J mol^{-1} K^{-1}), and T is the temperature (K).

Regeneration of Ni-NC: A 0.1 M NaOH solution was prepared and pumped into the reactor using a peristaltic pump at a flow rate of 4 mL min^{-1} without applying an electric current. After flushing for 20 min, the system was subsequently rinsed with deionized water at the same flow rate for 30 min, thereby achieving the *in-situ* regeneration of the catalyst.

2.3. Biological toxicity tests of degraded water samples

(1) **CCK-8 cell viability assay:** HepG2 cells were seeded in a 96-well plate at a density of 1×10^3 cells per well, with 100 μL of culture medium in each well. After 24 h incubation, the medium was replaced with 100 μL of different test solutions, including fresh culture medium (positive control, PC), pure water (blank control, BC), untreated water sample, and electrochemically treated water sample. Following another 24 h incubation, the medium was removed, and the cells were gently washed twice with phosphate buffer solution. Then, 10 μL of CCK-8 reagent was added to each well and incubated for 2 h. The absorbance at 450 nm was measured using a microplate reader, and cell viability was calculated according to Eq. (9).

$$cell\ viability(\%) = \frac{OD\ value(experimental\ group)}{OD\ value(control\ group)} \times 100\% \quad (9)$$

(2) **Mung bean germination assay:** Uniform and plump mung beans were selected, rinsed thoroughly with deionized water, and soaked at room temperature for approximately 6 h. Twenty seeds were then placed evenly at the bottom of clean beakers, followed by the addition of 10 mL of the corresponding test solution, ensuring sufficient contact without complete submersion. The experimental groups included pure water (blank control), untreated water sample, and electrochemically treated water sample. Cultivation was carried out in the dark at room temperature (~25°C), with the test solutions refreshed every 24 h to maintain stable conditions. Germination and growth were monitored over a 6-day period. At the end of cultivation, the stem length and fresh weight of the seedlings were measured.

3. Results and discussion

3.1. Material characterizations

To conduct a detailed analysis of the structure and surface characteristics of the molded Ni-NC_x materials, systematic characterizations were performed. As shown in Fig. 1a, the construction of the materials was based on a nickel foam-confined pyrolysis strategy. During the heating process, the polycondensation and cracking of melamine produced nitrogen-rich precursor gases, which *in situ* grew into nitrogen-doped carbon nanofibers under the catalytic effect of the nickel skeleton [38]. Concurrently, the HCl released from the thermal decomposition of NH_4Cl exerted a micro-etching effect on the nickel foam surface [38]. This not only promoted the local exfoliation and redispersion of Ni species but also provided a high density of defect sites for the nucleation of carbon fibers [38,39]. Ultimately, the resulting electrode macroscopically inherited the three-dimensional interconnected channels of the nickel foam. This monolithic self-supported structure effectively prevented the aggregation and loss of powder catalysts typically encountered in flow-through systems, and its inherent flexibility facilitated tight contact with the electrode [38]. Scanning electron microscopy (SEM) and transmission electron microscopy (TEM) images revealed that the interior of the Ni-NC_x materials contained abundant carbon nanofibers, forming a loose and porous structure (Fig. 1b and c). This architecture provided ample sites for adsorption and reactions. High-resolution TEM (HRTEM, Fig. 1d) demonstrated that ultrafine Ni nanoparticles, with sizes ranging from 1 to 2 nm, were highly uniformly confined or encapsulated within the carbon matrix. Energy-dispersive X-ray spectroscopy (EDS) elemental mapping (Fig. 1e and Fig. S4) indicates a relatively uniform distribution of Ni, C, and N within the carbon framework, without apparent large-scale aggregation of metal species.

To investigate the chemical state and local structure of Ni species, X-ray absorption fine structure (XAFS) and X-ray photoelectron spectroscopy (XPS) were employed. The Ni K-edge XANES spectrum shows that the absorption edge of Ni-NC_{50} lies between those of Ni foil and NiO, suggesting the coexistence of metallic and oxidized Ni species (Fig. 1f). The Fourier-transformed EXAFS spectra exhibit a dominant peak at ~2.02 Å, which can be assigned to Ni-Ni coordination (Fig. 1g), indicating that metallic Ni nanoparticles are the main Ni species in the material. This observation is consistent with the metallic Ni diffraction peaks observed in the XRD patterns (Fig. 1h) [40].

The surface composition and chemical states of the materials were analyzed by the high-resolution XPS. Despite varying the mass ratio of melamine to nickel foam (40-60), the surface contents of Ni (0.59-1.03 at.%) and O (0.77-1.22 at.%) remained relatively stable. The Ni 2p spectra show the coexistence of Ni^0, Ni^{2+}, and Ni^{3+} species (Fig. 1i), suggesting the presence of multiple oxidation states of Ni in the material [41]. Such multivalent Ni species are generally considered to facilitate interfacial electron transfer during the electrocatalytic process. In addition, the surface nitrogen content ranges from 5.74 to 7.69 at.%,

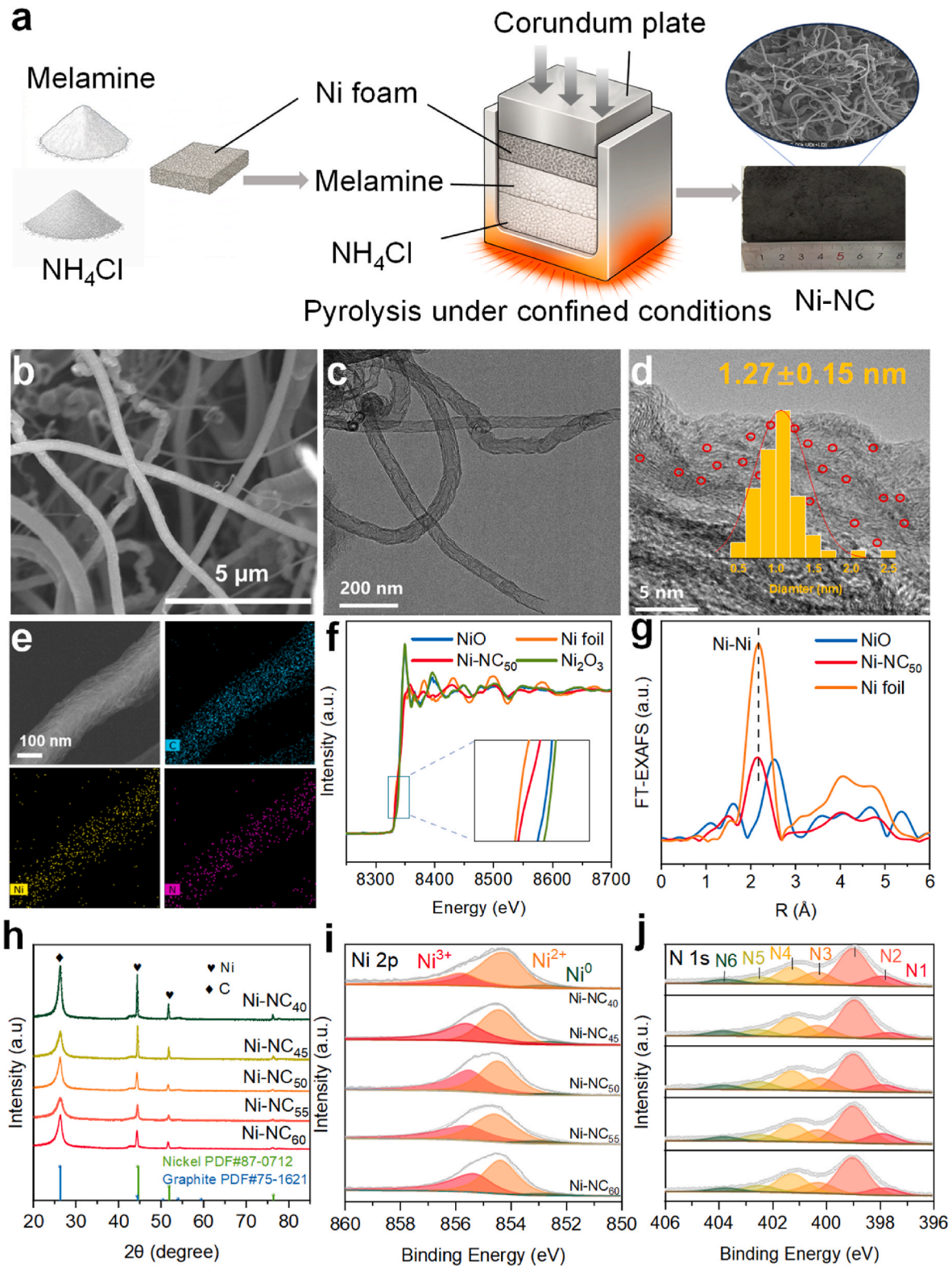

Fig. 1. (a) Schematic illustration of the synthesis of Ni-NC_x. (b) SEM image of Ni-NC_{50}. TEM (c) and HRTEM (d) images of Ni-NC_{50}. (e) EDS elemental mapping images of Ni, C, and N for Ni-NC_{50}. (f) Normalized Ni K-edge XANES spectra. (g) Fourier-transformed Ni K-edge EXAFS spectra. (h) XRD patterns of Ni-NC_x. Ni 2p (i) and N 1s XPS spectra (j) of Ni-NC_x.

indicating effective nitrogen incorporation into the carbon framework. The high-resolution N 1s spectra can be deconvoluted into several nitrogen species (Fig. 1j), including pyridinic N, pyrrolic N, graphitic N, N-oxide, and chemisorbed N, Notably, a characteristic peak at 398.9 eV is assigned to Ni-N_x coordination [41], suggesting the interaction between Ni species and the N-doped carbon matrix. This interaction may modulate the local electronic environment of Ni sites and influence their interaction with oxygen- or chlorine-containing intermediates during the reaction [42–44].

Contact angle measurements show that water droplets can rapidly

spread on the material surface, indicating good surface wettability (Fig. S5). This behavior is likely related to the presence of oxygen-containing functional groups, which introduce polar sites on the carbon framework. Such a hydrophilic surface facilitates the penetration of the TC solution into both the external surface and internal porous structure of the electrode. As a result, the accessibility of reactants to the catalytic sites is improved, which may help enhance mass transport and promote effective interaction between TC molecules and the active sites.

3.2. Catalytic performance

To evaluate the application potential of the self-supported Ni-NC_x electrodes, a circulating flow-through electrocatalytic degradation system was constructed (Fig. 2a). Unlike the traditional flow-by configuration, this device directed the TC-containing wastewater to pass vertically through a 5-mm-thick three-dimensional porous catalyst layer. At a volumetric flow rate of 1 mL min^{-1}, the fluid space velocity was 3076.92 h^{-1}, and the effective pore volume was 0.13 cm^3 g^{-1}, corresponding to a single hydraulic retention time of 1.17 s (Table S1). This convection-enhanced mode compressed the fluid boundary layer thickness at the solid-liquid interface, overcoming the mass transfer diffusion limitations of traditional systems [14].

For the effect of the interfacial physicochemical properties on electrocatalytic activity, the structural parameters and degradation performance of the Ni-NC_x materials synthesized with different precursor ratios were compared (Table 1). The results showed that as the melamine addition ratio increased, both the catalytic performance and structural parameters exhibited a volcano-shaped trend. When the mass ratio of melamine to nickel foam increased from 40 to 50, the TC removal efficiency increased from 68.99% to 95.82%, the COD removal percentage increased from 43.03% to 64.93%, and the reaction rate reached a peak of 0.11 mmol L^{-1} s^{-1}. Along with the increased catalytic

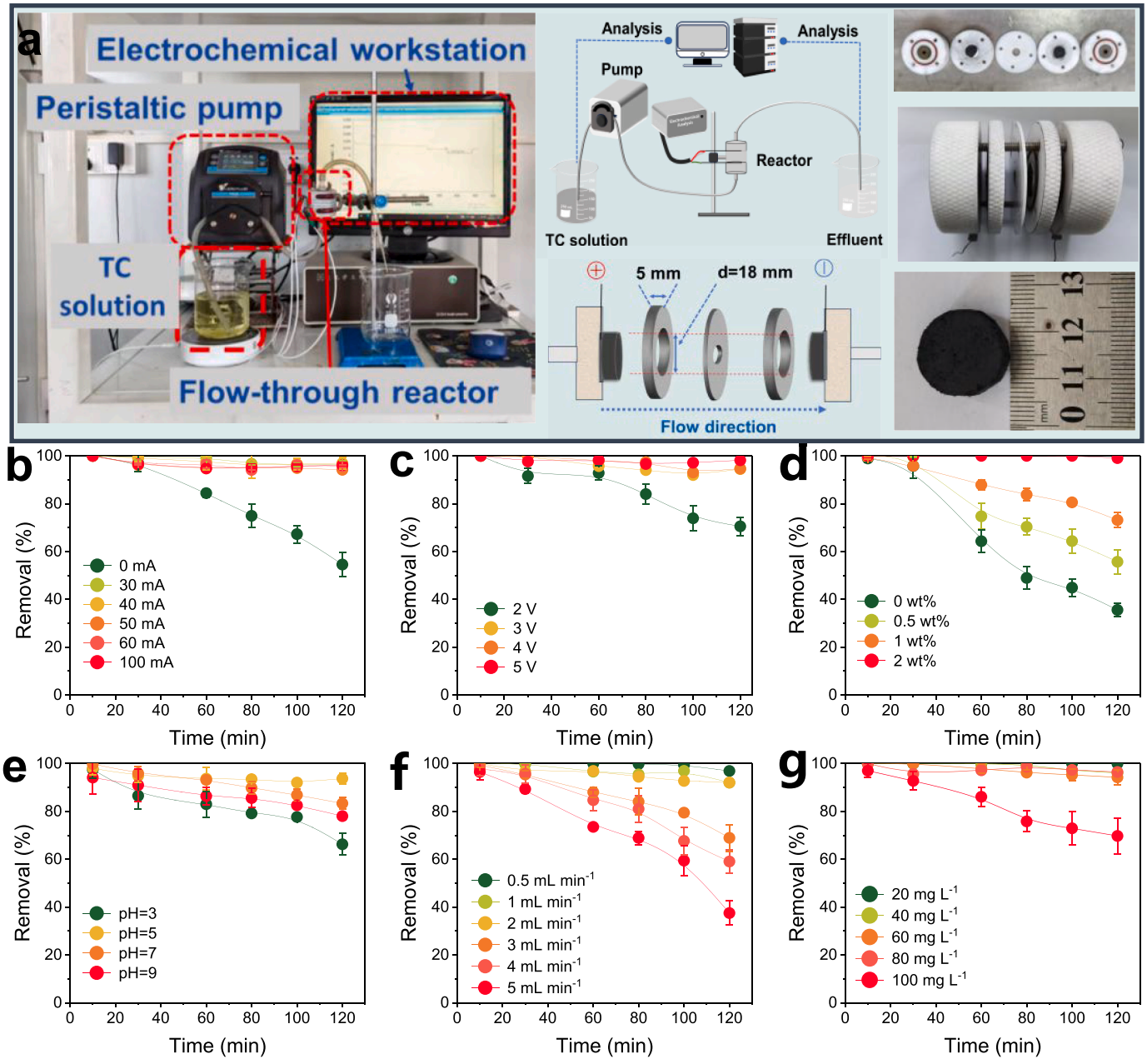

Fig. 2. (a) Schematic of the flow-through electrochemical system and reactor configuration. Effects of (b) applied current, (c) applied voltage, (d) electrolyte concentration, (e) initial pH, (f) flow rate, and (g) initial TC concentration on the TC removal efficiency.

Table 1
Degradation performance of TC over different materials in the self-designed reactor with a Flow-through operation.[a].

Materials	SSA[b] (m^2 g^{-1})	I_D/I_G[c]	XPS analysis [d] (at. %)			R_E[e] (mmol·L^{-1}·s^{-1})	X[f] (%)	X_{COD}[g] (%)	E_{COD}[h] (kWh kg^{-1} COD)	ACE[i] (%)	Refs
			Ni	N	O						
Blank[j]	31.77	1.23	1.03	7.69	0.92		58.22	58.22	-	-	-
Ni-NC_{40}	24.92	0.96	0.59	5.74	1.01	$7.72*10^{-2}$	68.99	43.03	62.24	24.16	-
Ni-NC_{45}	26.70	1.04	0.75	6.22	0.77	$9.52*10^{-2}$	88.57	50.21	46.57	27.47	-
Ni-NC_{50}	31.77	1.23	1.03	7.69	0.92	0.11	95.82	64.93	38.27	30.42	-
Ni-NC_{55}	27.69	1.20	0.96	7.55	1.22	0.11	95.37	55.10	44.84	28.32	-
Ni-NC_{60}	26.48	1.19	0.97	7.62	0.85	0.11	89.26	50.23	49.55	23.65	-
Ni-NC_{50}-Acid	25.44	1.05	0.48	5.73	1.25	0.04	33.42	10.77	57.04	5.43	-
GBC[k]	6.331	-	-	-	-	$3.37*10^{-5}$	99.48	66.61	81.9	-	[46]
ACF[l]	1219.3	-	-	-	-	$2.34*10^{-3}$	88	34.7	63.18	-	[47]
PCF[m]	0.52	-	-	-	-	$2.49*10^{-4}$	96	55.21	73.72	-	[48]
NiO@Co_3O_4/Ti[n]	-	-	-	-	-	$1.65*10^{-4}$	94.26	49.77	69.07	-	[49]
Ti/$NiCo_2O_4$/MnO_2[o]	-	-	-	-	-	$1.04*10^{-4}$	93.1	70.12	25.89	-	[50]

[a] Conditions: 2*0.15 g catalyst, 1 mL min^{-1}, 80 mg L^{-1} TC, pH = 5, 2 wt% NaCl solution, 50 mA,2 h.
[b] Specific surface area, data from N_2 adsorption-desorption isotherms of Ni-NC_x (Fig. S6).
[c] Data from the Raman spectra results (Fig. S7).
[d] Data from the XPS spectra results (Fig. S8).
[e] The electrocatalytically driven reaction rate.
[f] The TC removal efficiency, data from Fig. S9.
[g] COD removal percentage.
[h] Specific energy consumption.
[i] Average current efficiency.
[j] Without an applied electric field.
[k] GBC: graphene/biochar. Conditions:5 mg L^{-1} TC, pH = 9, 5 V, 0.2 M Na_2SO_4.
[l] ACF: active carbon felt. Conditions: 50 mg L^{-1} TC, 7 mL min^{-1}, pH = 3, 80 mA, 0.05 mol L^{-1} Na_2SO_4.
[m] PCF: polyacrylonitrile-based carbon fiber. Conditions: 70 mg L^{-1}, pH = 7, 15 mA cm^{-2}, 5 mmol L^{-1} PMS.
[n] Conditions: 100 mg L^{-1} TC, 0.25 mol L^{-1} NaCl, 48 mA cm^{-2}, pH = 7.88.
[o] Conditions: 30 mg L^{-1}, 40 mA cm^{-2}, pH = 5, 0.1 mol L^{-1} Na_2SO_4, pH = 5.

activity, the energy efficiency for pollutant mineralization improved. Ni-NC_{50} showed the lowest specific energy consumption for COD removal (38.27 kWh kg^{-1} COD) and the highest apparent current efficiency (ACE) of 30.42%. Compared with Ni-NC_{40} (E_{COD}: 62.24 kWh kg^{-1} COD, ACE: 24.16%), Ni-NC_{50} achieved a higher degree of pollutant removal in a shorter time, reducing the electrical energy loss caused by side reactions (such as the oxygen evolution reaction) [14,45]. This performance improvement was mainly attributed to structural optimization. At this ratio, the specific surface area (SSA) reached a maximum of 31.77 m^2 g^{-1}, providing space for liquid-solid interfacial reactions. Concurrently, the defect degree (I_D/I_G = 1.23) and nitrogen doping level (7.69 at.%) reached their highest values. Furthermore, the introduction of the nitrogen-rich precursor facilitated the anchoring and dispersion of active Ni species (1.03 at.%) within the carbon skeleton. However, when the mass ratio further increased (e.g., Ni-NC_{60}), excessive precursor pyrolysis caused the carbon nanofibers to entangle and locally densify. This led to pore structure collapse and steric hindrance (SSA decreased to 26.48 m^2 g^{-1}), resulting in a decrease in the TC removal efficiency to 89.26% and the COD removal percentage to 50.23%. The decrease in activity led to lower energy utilization efficiency; the E_{COD} of Ni-NC_{60} increased to 49.55 kWh kg^{-1} COD, while the ACE decreased to 23.65%.

The identification of the source of surface activity is crucial. Here, Ni-NC_{50} was washed with acid (denoted as Ni-NC_{50}-Acid) to remove detachable nickel species. As shown in Table 1, acid washing removed a portion of the exposed Ni-containing components (Ni content decreased to 0.48 at.%). With the skeleton specific surface area remaining largely unchanged, the degradation activity of the system decreased: the TC removal efficiency dropped to 33.42%, and the R_E value decreased to 0.039 mmol L^{-1} s^{-1}. Meanwhile, the E_{COD} increased to 57.04 kWh kg^{-1} COD, and the ACE remained at 5.43%. This result indicated that the metallic active centers composed of multivalent Ni and Ni-N_x were the primary active sites driving the reaction [51,52]. The relative contents of key surface active species were further quantified (Fig. 4b, Figs. S10 and S11). The results showed that acid etching caused a loss of surface components. Although graphitic N (serving as the conductive framework) and Ni-N_x (providing coordinate anchoring) retained 75.3% and 68.2% of their original contents, respectively, the high-valence nickel particles and Ni^{3+} species at the interface decreased by 67.5%. This suggested that nickel particles, especially Ni^{3+} species, acted as the key intrinsic oxidation sites. The system developed in this study was quantitatively compared with benchmark carbon-based and metal oxide electrodes reported in recent literature. Due to the mass transfer enhancement by the flow-through configuration and the reduction of the reaction energy barrier by Ni active sites, the apparent reaction rate of Ni-NC_{50} was 2 to 3 orders of magnitude higher than that of traditional powder or bulk electrodes. Maintaining the removal efficiency, Ni-NC_{50} showed lower energy consumption. Its processing energy consumption (E_{COD}) was 38.27 kWh kg^{-1} COD, which was lower than that of many catalytic materials (e.g., GBC: 81.9 kWh kg^{-1} COD; ACF: 63.18 kWh kg^{-1} COD), and it achieved an ACE of 30.42%. Moreover, to comprehensively benchmark the practical engineering superiority of the self-supporting Ni-NC50 electrode, its catalytic performance was compared with recently reported state-of-the-art electrochemical advanced oxidation systems as well (Table S2). While conventional Electro-Fenton and Electro-Oxidation-Persulfate processes achieve commendable degradation, they are heavily constrained by the requisite continuous dosing of external chemicals (e.g., Fe^{2+}, PMS) and the necessity for harsh acidic environments (pH 2–3) to prevent metal precipitation or activate persulfates. In striking contrast, the Ni-NC50 flow-through system operates efficiently under a mildly acidic condition (pH 5) without the addition of any external oxidants, ingeniously leveraging the inherent high-salinity matrix (2 wt NaCl) for in-situ radical/active chlorine generation. Furthermore, while most reported literature evaluates relatively low or trace-level TC concentrations (10–60 mg/L) in static batch reactors, our system achieved exceptional removal (95.82%) and robust deep mineralization (64.93% COD removal) against a massively concentrated organic load (80 mg/L) under a continuous high-throughput flow regime. This comparative

analysis explicitly highlights that the Ni-NC_{50} flow-through architecture provides a highly scalable, low-chemical-footprint, and energy-efficient paradigm for the continuous remediation of hyper-concentrated industrial effluents.

While the flow-through configuration undoubtedly enhances macroscopic external diffusion, its profound impact lies in the modulation of the internal microenvironment of the porous electrode. As elegantly highlighted in recent milestone studies regarding single-atom and porous electrocatalysis [53], the local interfacial microenvironment, spatial confinement, and internal concentration distribution dictate the ultimate catalytic performance. In conventional flow-by modes, severe internal diffusion resistance leads to reactant depletion deep within the pores, produced non-active zones and triggering parasitic side reactions. In our system, the 3D hierarchical Ni-NC_{50} scaffold functions as a spatial flow distributor. The forced permeation continuously drives the hypersaline electrolyte into the spatially confined micropores, shattering the internal Nernst diffusion layers.

The input current and voltage determine the interfacial electron transfer rate and the amount of reactive species generated [54]. As shown in Fig. 2b, under the open-circuit condition (0 mA), 58.22% of TC was captured via physical adsorption after 2 h. This high adsorption capability of carbon adsorbent would benefit the enrichment of TC on the surface, facilitating the degradation process. Upon applying a current of 30 mA, the removal efficiency increased to 98.82%, indicating the role of the electric field in the degradation process. At this point, the COD removal percentage was 40.54% (Fig. S12), indicating the accumulation of organic intermediate molecules that underwent ring-opening or bond cleavage but were not fully mineralized. As the current was further increased to 60 mA and 100 mA, the COD removal percentage rose to 81.74%, achieving organic mineralization. However, the increased current caused the ACE to decrease from 30.43% to 14.25%, while the E_{COD} increased to 71.32 kWh kg^{-1} COD. This suggested that under high overpotentials, a portion of the input charge was consumed by side reactions (such as the OER, and the hydrogen evolution reaction, HER), leading to a lower ACE. Constant-voltage tests (Fig. 2c) further supported this observation: although a constant voltage of 4 V achieved a mineralization degree of 86.69% (Fig. S13), its E_{COD} was 88.31 kWh kg^{-1} COD. To balance degradation kinetics and energy consumption, a constant current of 60 mA was determined to be the optimal energy input mode.

In the electrocatalytic treatment of saline wastewater, coexisting anions affect the anodic oxidation pathways. As shown in Fig. 2 d, without the NaCl electrolyte, the TC removal efficiency was 33.65% due to the solution ohmic potential drop. After introducing Cl^-, the reaction activity increased. When the Cl^- concentration reached 2 wt%, the TC removal efficiency was 99.05%. This improvement was attributed to the enhanced solution conductivity and the fact that the concentration of Cl^- triggered the CER at the Ni active sites [55]. This induced the generation of RCS [56,57] with long lifetimes and selectivity, increasing the concentration of oxidizing radicals in the bulk solution. The initial pH of the solution determined the thermodynamic steady-state distribution of the RCS (Fig. 2e). The system showed the highest activity (92.07%) under weakly acidic conditions (pH = 5). This was because free active chlorine primarily existed as hypochlorous acid (HClO, standard electrode potential $E_0 = 1.63$ V) in this environment. As the solution became more alkaline, HClO gradually converted to ClO^- ($E^0 = 0.89$ V), which is generally considered to have a lower oxidation capacity, leading to a decline in degradation efficiency. Under strongly acidic conditions (pH = 3), a reduced removal efficiency (69.46%) was observed. This behavior may be related to the HER at the cathode, where the generation of gas bubbles could hinder the contact between the solution and the electrode surface, thereby affecting mass transport within the porous structure.

The flow rate plays an important role in determining the effective contact time and mass transfer behavior between pollutants and the catalytic interface [14]. As shown in Fig. 2f, when the flow rate increased from 1 to 5 mL min^{-1}, the removal efficiency decreased from 92.04% to 41.09%. Although a higher flow rate can enhance convective mass transfer, the corresponding decrease in residence time limits the interaction between TC molecules and active sites. As a result, part of the TC may pass through the electrode channels without sufficient oxidation. The concentration effect experiment (Fig. 2g) showed that the system maintained a removal capacity of nearly 100% within the concentration range of 20–80 mg L^{-1}. When the concentration reached 100 mg L^{-1}, the limited number of surface active centers could not match the higher content of organic substrates. Coupled with the competitive adsorption of intermediate products, the removal efficiency decreased to 75.44%. Considering the space-time yield and retention efficiency, 1 mL min^{-1} and 80 mg L^{-1} were determined to be the suitable hydrodynamic and mass loading boundary conditions. It should be noted that the initial TC concentration employed in this study (80 mg/L) was deliberately selected to simulate highly concentrated industrial and agricultural point-source effluents, rather than trace-level natural water bodies. Recent investigations regarding the distribution of antibiotics have revealed that TC concentrations in pharmaceutical wastewater treatment plant effluents can reach up to 32.0 ± 6.0 mg/L [58]. Moreover, extreme accumulation of TCs in agricultural feeds (up to 71.8 mg/kg) and dewatered sludge (up to 5481 mg/kg) generates highly concentrated flushing wastewaters and leachates. In actual engineering practice, such point-source effluents often undergo pre-concentration (e.g., reverse osmosis), further elevating the local concentration. Therefore, evaluating the electrocatalytic system at 80 mg/L rigorously tests its upper-limit oxidation capacity and practical viability for decentralized source control of hyper-concentrated antibiotic streams.

To evaluate the matrix robustness of the Ni-NC_{50} flow-through system, ubiquitous inorganic ions (at a stringent concentration of 50 mM) were introduced into the reaction (Fig. S14). For anions, SO_4^{2-} and NO_3^- exhibited negligible interference, whereas HCO_3^- moderately decreased TC removal owing to the classical scavenging of highly reactive •OH into less oxidative carbonate radicals. Interestingly, divalent cations (Mg^{2+} and Ca^{2+}) drastically suppressed the degradation kinetics compared to monovalent K^+. This pronounced inhibition is mechanistically attributed to a dual effect: (i) strong complexation between Mg^{2+}/Ca^{2+} and the oxygen-rich moieties of TC, which sterically and electronically shields the pollutant from oxidative attack; and (ii) the compression of the electric double layer by high-valence cations at the solid-liquid interface, which further hinders the mass transfer of reactants. Consequently, matrix inhibition is a synergistic result of radical scavenging, metal-pollutant complexation, and interfacial charge regulation.

Furthermore, to rigorously evaluate the degree of deep mineralization and exclude potential oxidative interferences from the hypersaline matrix, TOC analysis was performed (Fig. S15). Under optimal flow-through conditions, the TOC concentration significantly decreased from 40.7 mg C/L to 16.2 mg C/L, achieving an outstanding TOC removal efficiency of 60.18%. This efficiency is logically slightly lower than the COD removal rate (64.93%), as complete decarboxylation into CO_2 (measured by TOC) involves a higher energetic barrier than partial molecular fragmentation. Nevertheless, this substantial TOC abatement firmly corroborates that the synergistic reactive network generated by the 3D Ni-NC_{50} anode profoundly drives genuine deep mineralization within a minimal hydraulic retention time.

3.3. Degradation mechanism investigation

In the electrocatalytic treatment of saline wastewater, the electron transfer at the anodic interface determines the generation pathway of reactive species [59]. To investigate the electrocatalytic degradation of TC by the self-supported Ni-NC_{50} system, the generation and role of reactive species in this process were analyzed. First, when Na_2SO_4 was used as the electrolyte, the TC removal efficiency after 2 h was 71.16%. In the NaCl system with equivalent ionic strength, the removal efficiency was 99.05% (Fig. S16). This difference indicated that Cl^- in the system

was not an inert supporting electrolyte but was activated to participate in the oxidative degradation process. To quantify the contributions of different active species, gradient radical quenching experiments were conducted. As shown in Fig. 3a, the addition of $Na_2S_2O_3$ (a quencher for free available chlorine, FAC) showed an inhibitory effect on the reaction. When the quencher concentration was 1 M, the removal efficiency decreased to 23.88% (higher than the 9.26% of pure adsorption), indicating that FAC played a primary role in this saline flow-through system. Meanwhile, the addition of methanol (an •OH quencher) reduced the removal efficiency to 59.91% (Fig. 3b), indicating that •OH was also an oxidation participant [60]. With the introduction of tert-butanol (TBA, a quencher for both •OH and chlorine radicals, CRs), the removal efficiency further decreased to 50.77% (Fig. S17). The stronger inhibitory effect of TBA compared to methanol confirmed the role of CRs (e.g., Cl•, $Cl_2•^-$) in the radical oxidation pathway [61]. In situ EPR trapping was used to analyze the evolution of the species. In the Cl^--free system, a characteristic four-line signal of DMPO-•OH with an intensity ratio of 1:2:2:1 was detected (Fig. 3c, AN = AH = 14.9 G), confirming the single-electron activation of water molecules at the Ni active sites [62]. However, upon the introduction of Cl^-, the spectrum transformed into a typical seven-line signal (Fig. 3d), which was assigned to the DMPO-X signal formed by the irreversible oxidation of DMPO by oxidizing chlorine-containing species [63]. This transition from the DMPO-•OH to the DMPO-X signal indicated the occurrence of the CER at the anodic interface, showing that •OH could initiate the chain reaction of Cl^- to form RCS [60]. As previously pointed out, the high initial physical adsorption (58.22%) played a pivotal role in the overall reaction rate. Rather than acting as a mere phase-transfer sink, the hierarchical Ni-NC50 framework operated via a robust enrichment-degradation process. The pronounced physical and electro-adsorption capacities rapidly concentrated TC molecules at the solid-liquid interface. Subsequently, the *in-situ* generated high-flux reactive species (FAC and •OH) promptly oxidize the localized TC, continuously liberating the active sites. This dynamic equilibrium ensures that while adsorption initiates the capture, the electrocatalytic degradation irreversibly drives the continuous mass removal, as evidenced by the sustained efficiency over the continuous flow-through operation (Fig. 2b).

To ensure the rigor of the proposed mechanism, the potential involvement of other reactive species, specifically sulfate radicals ($SO_4^{\bullet-}$) and singlet oxygen ($^1O_2$), was critically evaluated. Although Na_2SO_4 was utilized as an inert supporting electrolyte during the •OH-EPR trapping to prevent chlorine interference, no characteristic DMPO- SO_4 signals

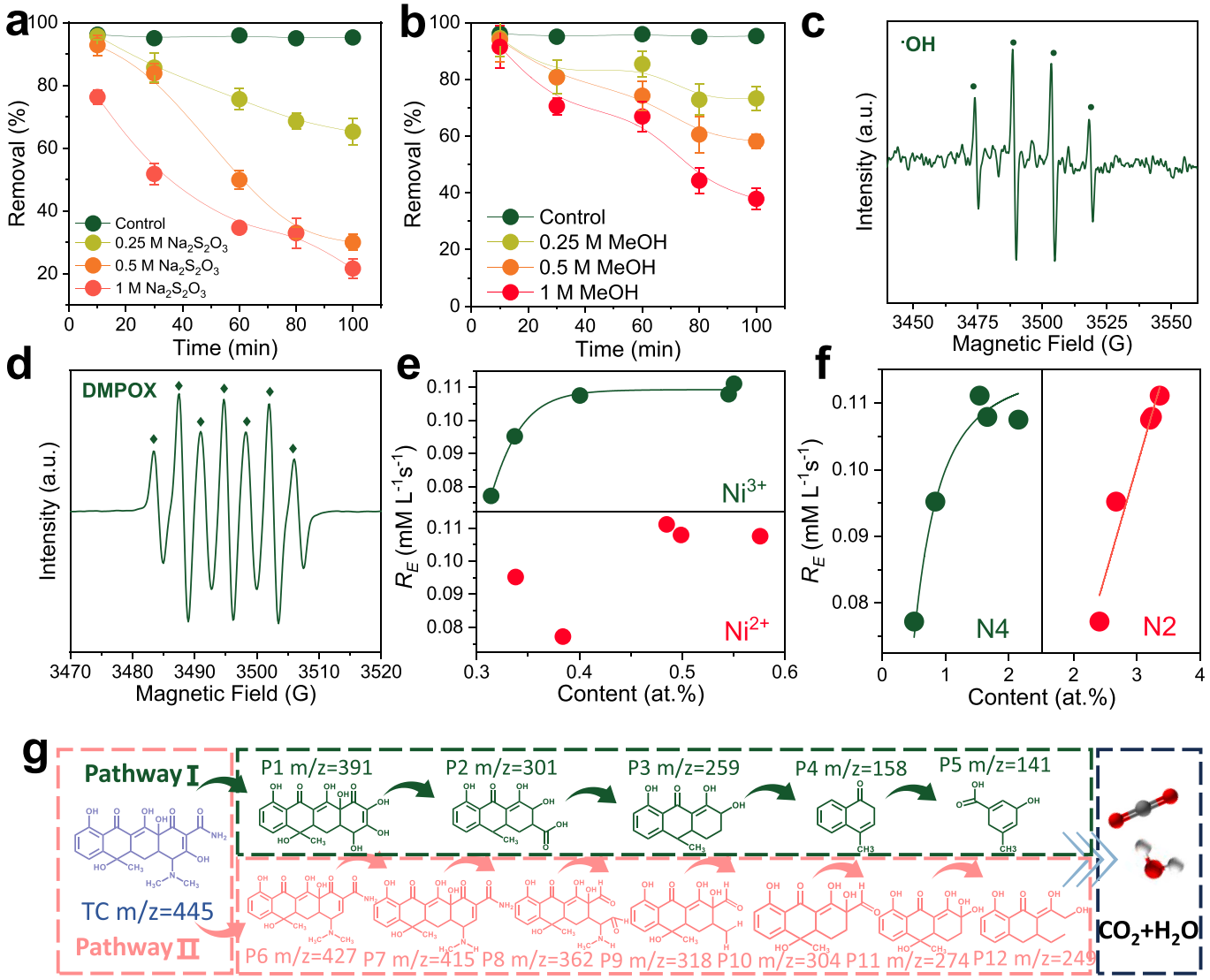

Fig. 3. (a) Effect of the $Na_2S_2O_3$ quencher on TC degradation. (b) Effect of the methanol quencher on TC degradation. (c) EPR spectrum of the DMPO-•OH adduct. (d) EPR spectrum of DMPO-X. (e) Correlation between the relative contents of Ni valence states and the reaction rate. (f) Correlation between the nitrogen species (N4 and N2) and the reaction rate. (g) Proposed degradation pathways for TC.

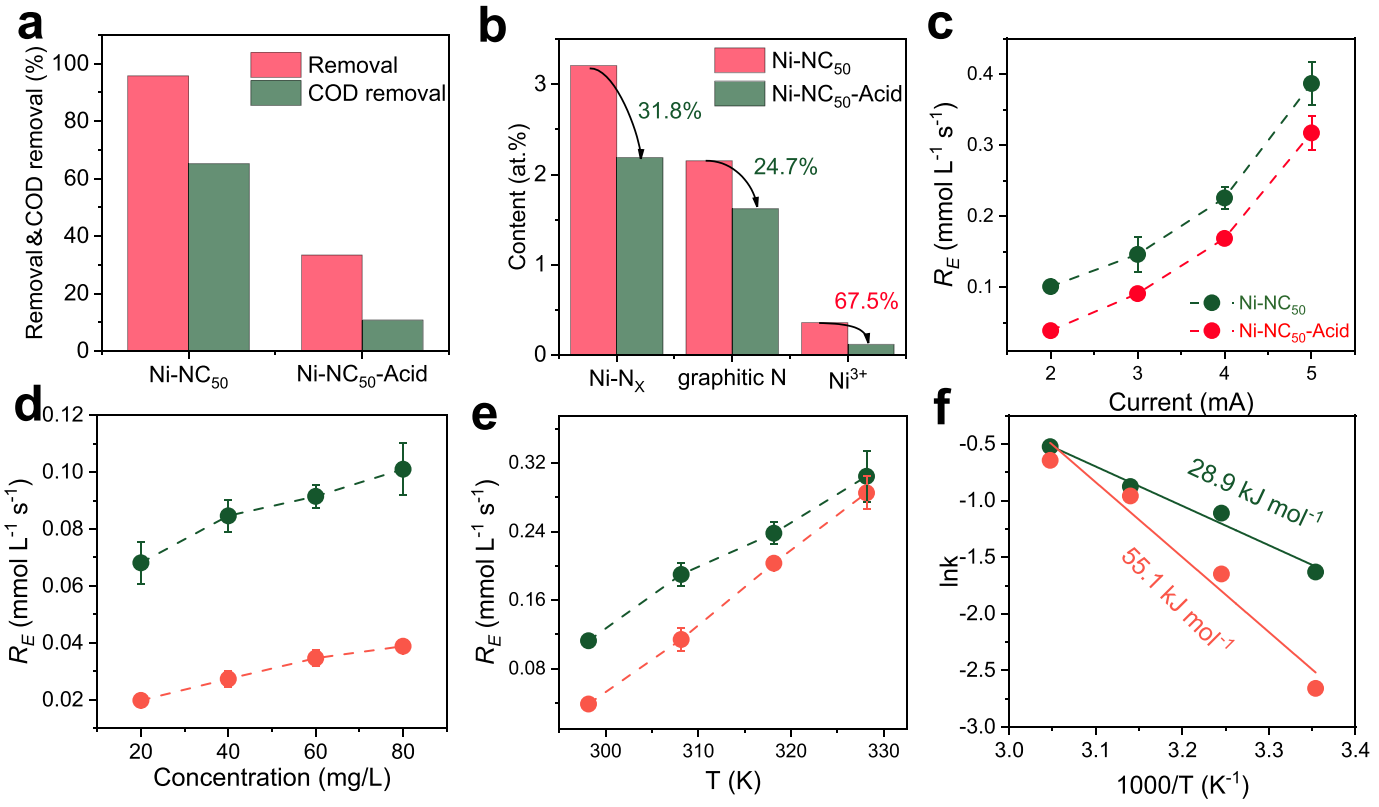

Fig. 4. Activity (a) and variation of key active species (b) of the pristine and acid-washed one. Dependence of reaction rate on applied current (c), initial concentration (d), and reaction temperature (e) over both catalysts. (f) Arrhenius plots of both catalysts in this process.

were detected. This is thermodynamically consistent, as the direct anodic oxidation of SO_4^{2-} requires ultra-high overpotentials typically achievable only on BDD or specific metal oxides [64], rather than carbon-based anodes. Thus, $SO_4^{\bullet-}$ is not generated in this system. Furthermore, the generation of $^1O_2$ was investigated using TEMP-EPR and L-Histidine (L-His) quenching (Fig. S18). The TEMP-EPR spectrum exhibited no characteristic signals, definitively ruling out the presence of $^1O_2$. While the addition of L-His severely inhibited TC degradation, this phenomenon is identified as a false-positive interference. L-His, owing to its amine and imidazole groups, is highly susceptible to rapid electrophilic attack by free available chlorine (FAC) and •OH. Therefore, the apparent inhibition stems from the massive competitive consumption of the primary oxidants (FAC and •OH) by L-His, rather than the quenching of $^1O_2$. These comprehensive validations firmly substantiate that the dynamically interconverting FAC/•OH network acts as the dominant reactive pathway driving the electrocatalytic degradation under the investigated conditions, while the contribution of $^1O_2$ remains negligible.

The highly efficient in-situ generation of FAC from the chloride-rich matrix significantly drives the degradation process. This aligns perfectly with recent studies emphasizing that the judicious selection of anodic materials can ingeniously convert ubiquitous chloride ions into potent reactive chlorine species, thereby enabling sustainable decentralized remediation without external chemical dosing [9]. Furthermore, the observed radical scavenging by HCO_3^- and the resulting kinetic inhibition corroborate recent findings on the complex matrix effects in authentic wastewater environments, where ubiquitous inorganic species critically govern the distribution of reactive radicals.

While EPR spin-trapping qualitatively identified the generated radicals, the hypersaline anodic environment fosters a complex, dynamically interconverting oxidant network. To quantitatively decouple their relative contributions, the generation of FAC was first evaluated (Fig. S19a), revealing a robust and steady FAC output of up to ~ 1.92 mg/L within the ultra-short residence time. Subsequently, the hydraulic retention times (HRT)-dependent kinetic evaluations were performed under various radical scavenging scenarios (Fig. S19b and c). In the unquenched system, the baseline k_{obs} reached an exceptional 15.21 s^{-1}. The independent addition of methanol (scavenging •OH) and $Na_2S_2O_3$ (scavenging FAC/RCS) reduced the k_{obs} by 36.03% and 72.65%, respectively. Furthermore, the simultaneous addition of both scavengers resulted in an overall kinetic inhibition of 76.92%.

These precise quantitative metrics provide profound mechanistic insights into the degradation pathway. First, the fact that the combined inhibition (76.92%) leaves a residual ~ 23% of unquenched kinetics explicitly confirms the coexistence of direct anodic oxidation. Facilitated by the strong π-π pre-enrichment capability of the 3D Ni-NC scaffold, a portion of the densely adsorbed TC molecules undergoes direct electron transfer at the Ni active sites without relying on diffusible oxidants. Second, the sum of the individual inhibitory contributions (36.03% + 72.65% = 108.68%) explicitly exceeds both 100% and the combined quenching limit (76.92%). This kinetic overlap provides robust quantitative evidence for the dynamic interconversion between reactive species under strong anodic polarization. Specifically, the highly oxidative •OH inevitably reacts with the abundant Cl^- background via the dynamic equilibrium: $\bullet OH + Cl^- \leftrightarrow ClOH^{\bullet-} \leftrightarrow Cl^{\bullet} + OH^-$, cascading into secondary highly reactive chlorine radicals. Conclusively, this kinetic decoupling definitively verifies that the Ni-NC electrocatalyst operates via a profoundly synergistic mechanism, wherein the direct anodic electron transfer is intricately coupled with a dynamically interconverting •OH/RCS homogeneous oxidant network, collectively enabling the ultra-fast mineralization of TC.

It should be noted that the EPR detection was purposefully conducted in a static 0.1 M Na_2SO_4 cell to unmask the intrinsic •OH generation by eliminating the severe oxidative interference from active chlorine. Under the identical applied current (60 mA), the anodic potential in this static model reached +2.2 to +2.5 V vs. Ag/AgCl. In the

actual two-electrode flow-through degradation system (20 g/L NaCl), the total cell voltage was recorded at 3.2–3.4 V. Deducting the estimated cathodic hydrogen evolution overpotential, the true anodic polarization potential in the flow-through system is thermodynamically comparable (+2.0 to +2.3 V). The marginally lower polarization in the flow-through system is mechanistically reasonable, attributed to the significantly enhanced electrolyte conductivity and forced convection, which mitigate mass-transfer resistance. Therefore, the •OH generation identified in the EPR test is thermodynamically and mechanistically representative of the actual degradation system.

Investigating the correlation between the material microstructure and its activity helps to understand the role of surface active sites in the degradation process. Previous studies have reported that Ni-based materials can participate in the electrochemical oxidation process through reversible valence state transitions, acting in electron transfer and interfacial reactions [65]. Nitrogen doping in the carbon framework is generally considered to improve electrocatalytic performance by modifying the local electronic structure, enhancing electrical conductivity, and stabilizing metal species [65,66]. In addition, oxygen-containing functional groups on the surface may also influence the reaction behavior by affecting surface properties such as polarity and wettability [67]. For porous carbon electrodes, these surface characteristics could further impact the accessibility of reactants and the interfacial reaction environment within the pore structure [68]. In flow-through electrochemical systems, the overall reaction involves the coupling of mass transport and interfacial processes. Under such conditions, the relationship between material composition, surface characteristics, and catalytic performance becomes particularly important. As shown in Fig. S20, both Ni and N contents exhibit positive correlations with the reaction rate, whereas no clear correlation is observed for O content. These results suggest that metal species and nitrogen functionalities are more closely associated with the electrocatalytic activity in this system, while the contribution of surface oxygen groups appears to be less pronounced. The O element in the material mainly originated from surface oxidation during air exposure and the electrochemical reaction, rather than being an intrinsic component of the precursors. Thus, its content tends to reflect changes in the surface state. To further analyze the chemical forms, the valence states of Ni species and the distribution of nitrogen species were evaluated using XPS. As shown in Fig. 3e, the apparent reaction rate of the system showed a nonlinear positive correlation with the relative content of surface Ni^{3+}, while the Ni^{2+} content showed a random distribution. This phenomenon indicated that high-valence Ni^{3+} acted as the core site driving the catalytic oxidation. Under an anodic potential, the Ni-OOH-like structure formed by the reconstruction of interfacial Ni species can lower the activation energy barrier for water and Cl^- oxidation [69]. The removal efficiency (R_E) also showed a positive correlation with the contents of Ni-N_x (N2) and graphitic nitrogen (N4) (Fig. 3f), whereas pyridinic nitrogen (N1) and pyrrolic nitrogen (N3) did not show a positive correlation (Fig. S21). From a coordination chemistry perspective, the construction of Ni-N_x induced a metal-support interaction [70]. The surrounding N atoms anchored the Ni nanoparticles and adjusted the d-band center position of the Ni active centers by attracting electrons, thereby promoting the transition of low-valence Ni to Ni^{3+}. Simultaneously, graphitic nitrogen provided an electron transport channel across the interface, ensuring low ohmic loss of the flow-through reactor at the applied current density and contributing to the electrocatalytic activity of Ni-NC_{50} [36,71,72].

To unambiguously identify the actual catalytic active sites and establish a robust structure-activity relationship, specific chemical poisoning experiments coupled with electrochemical and spectroscopic analyses were conducted. Potassium thiocyanate (KSCN), a potent masking agent known to specifically coordinate with transition metals, was utilized to poison the Ni centers. As depicted in Fig. S22a, after soaking the electrode in 0.1 M KSCN, the macroscopic degradation performance of the KSCN-Ni-NC_{50} electrode deteriorated drastically. To verify whether this decline was an artifact of pore blockage, the electrochemically active surface areas (ECSA) were quantified by extracting the double-layer capacitance from cyclic voltammograms (Fig. S22b–d). Especially, the pristine Ni-NC_{50} and the poisoned KSCN-Ni-NC_{50} exhibited nearly identical ECSA values (667.5 cm^2 and 682.5 cm^2, respectively). This critical equivalence explicitly confirms that the performance degradation is strictly independent of the physically accessible surface area, but stems entirely from the quenching of the intrinsic catalytic activity at the Ni sites. The microscopic origin of this catalytic deactivation was further elucidated via high-resolution XPS (Fig. S22e–f). In the Ni 2p spectrum of KSCN-Ni-NC_{50}, the binding energies exhibited a distinct positive shift relative to the pristine catalyst, indicating a substantial decrease in the local electron density around the Ni centers. This electron depletion is driven by the strong coordination of SCN^- ligands, which violently disrupts the original Ni-N-C electronic bridging and significantly weakens the electron donation/feedback from the N-doped carbon skeleton. Concurrently, the pronounced enhancement of the satellite peaks implies an increase in unpaired electrons, corresponding to the coordination reconstruction into Ni^{2+} species with unfilled 3d orbitals. Conclusively, the disruption of this delicate interfacial electronic structure, which directly led to macroscopic catalytic failure without altering the ECSA, definitively corroborates that the covalently coupled Ni-N_x configurations act as the indispensable active centers for the electrocatalytic oxidation process.

Based on the above mechanism, the main reaction network of TC in this saline flow-through system can be described as follows: under the catalysis of the Ni-N-C interface, Cl^- underwent a two-electron transfer to generate Cl_2, which hydrolyzed to produce FAC (Eqs. (10)–(12)) [56,57]. Concurrently, the generated •OH reacted with Cl^- through a single-electron reaction to produce CRs (Eqs. (13)–(16)) [73]. FAC and •OH/CRs acted together on the TC molecules. Further product analysis using ultra-performance liquid chromatography quadrupole time-of-flight mass spectrometry (UPLC-Q-TOF-MS) identified nine intermediate products (Fig. S23), based on which two parallel degradation pathways were proposed (Fig. 3g). FAC tended to attack the dimethylamino and phenolic hydroxyl functional groups in the TC structure, initiating deamidation, dehydration, and initial hydroxylation (e.g., the formation of P1). Subsequently, under the action of the generated radicals, the fused-ring skeleton of the TC molecule underwent ring-opening cleavage (e.g., P3, P6, P7), accompanied by decarboxylation and decarbonylation reactions. It was further degraded into small-molecule fatty acids until mineralization [74,75]. This analysis is consistent with the COD removal percentage observed in Section 3.2.

$$2Cl^- \rightarrow Cl_2 + 2e^- \quad (10)$$

$$Cl_2 + H_2O \rightleftharpoons HOCl + H^+ + Cl^- \quad (11)$$

$$HOCl \rightleftharpoons H^+ + OCl^- \quad (12)$$

$$H_2O \rightarrow \cdot OH + H^+ + e^- \quad (13)$$

$$Cl^- + \cdot OH \rightarrow Cl\cdot + OH^- \quad (14)$$

$$Cl\cdot + Cl^- \rightarrow Cl_2^- \quad (15)$$

$$TC + FAC\ /\ \cdot OH\ /\ CRs \rightarrow \text{intermediates} \rightarrow \text{smaller oxidation products} \quad (16)$$

3.4. Kinetic study

To investigate the role of the surface active sites of the Ni-NC catalyst in intrinsic catalytic activity from a microkinetic perspective, a comparative analysis of reaction kinetics was conducted using Ni-NC_{50} and the acid-washed material (Ni-NC_{50}-Acid) as models. As shown in Table 1, the activity of the acid-washed catalyst decreased due to the reduction of key active sites. Although the increase in applied current enhanced the electrochemical electron driving force for both systems,

leading to an upward trend in R_E, Ni-NC_{50} maintained higher kinetic activity (Fig. 4c). In this investigation, when an applied current of 5 mA, the R_E of Ni-NC_{50} reached 0.408 mmol L^{-1} s^{-1}, indicating that its active sites could facilitate electron transfer. In contrast, due to the lack of active centers, the increase in R_E for Ni-NC_{50}-Acid was limited (0.304 mmol L^{-1} s^{-1}), showing slower kinetics. A similar trend was observed in the response to substrate concentration (Fig. 4d). Under the same mass transfer driving force of concentration, Ni-NC_{50} exhibited higher reaction activity, whereas Ni-NC_{50}-Acid, lacking the metal active centers, showed limited capacity to capture and activate TC molecules, resulting in a lower overall reaction rate.

The activation energy is a direct indicator of the energy barrier in a catalytic reaction. As shown in Fig. 4e, when the temperature increased from 298 K to 328 K, the reaction rate of Ni-NC_{50}-Acid showed a strong temperature dependence, increasing by approximately 7 times. In comparison, the rate increase for Ni-NC_{50} was notably lower (approximately 3 times), indicating that its intrinsic reaction was less restricted by temperature changes. To further evaluate the temperature dependence of the reaction kinetics, the Arrhenius equation was applied to fit the relationship between the rate constant and temperature (Fig. 4f). The *E*a of the acid-washed sample was calculated to be 55.1 kJ mol^{-1}. For Ni-NC_{50}, which contained abundant Ni active centers, the *E*a of this process was significantly reduced to 28.9 kJ mol^{-1}. To ensure that this pronounced reduction in *E*a represents improved intrinsic catalytic kinetics rather than being convoluted with mass-transfer effects, the Arrhenius experiments were strategically evaluated under a strict kinetic control regime (i.e., a low current of 2 mA and a high flow rate of 10 mL min−1, with delayed steady-state sampling at 90–120 min) to obliterate external diffusion and adsorption interferences. Furthermore, Electrochemical Impedance Spectroscopy (EIS, Fig. S24) was employed. The low-frequency Warburg impedance tails exhibited nearly identical slopes for both Ni-NC_{50} and Ni-NC_{50}-Acid, explicitly confirming that the acid-leaching process did not alter the internal physical mass-transfer pathways. Meanwhile, the intrinsic series resistance (R_s) notably increased after acid washing, reflecting a disrupted localized electronic network. Having definitively ruled out mass-transfer artifacts, this substantial *E*a reduction strictly verifies that the synergy between the Ni-N_x coordination centers and high-valence Ni^{3+} intrinsically optimized the adsorption configuration of intermediates (e.g., Cl^-) at the interface. This inherently lowered the energy barrier of the rate-determining step for the CER and radical generation, which ultimately contributed to the excellent macroscopic degradation performance of the Ni-NC_{50} flow-through system.

3.5. Stability study

In a flow-through electrocatalytic system, the self-supported electrode is exposed to a directional electric field, oxidizing reactive species, and continuous fluid shear stress over extended periods. Therefore, the structural stability of the interface and the long-term lifespan of the catalyst are indicators for evaluating its industrial application potential [76,77]. To this end, continuous cycling and long-term operation of

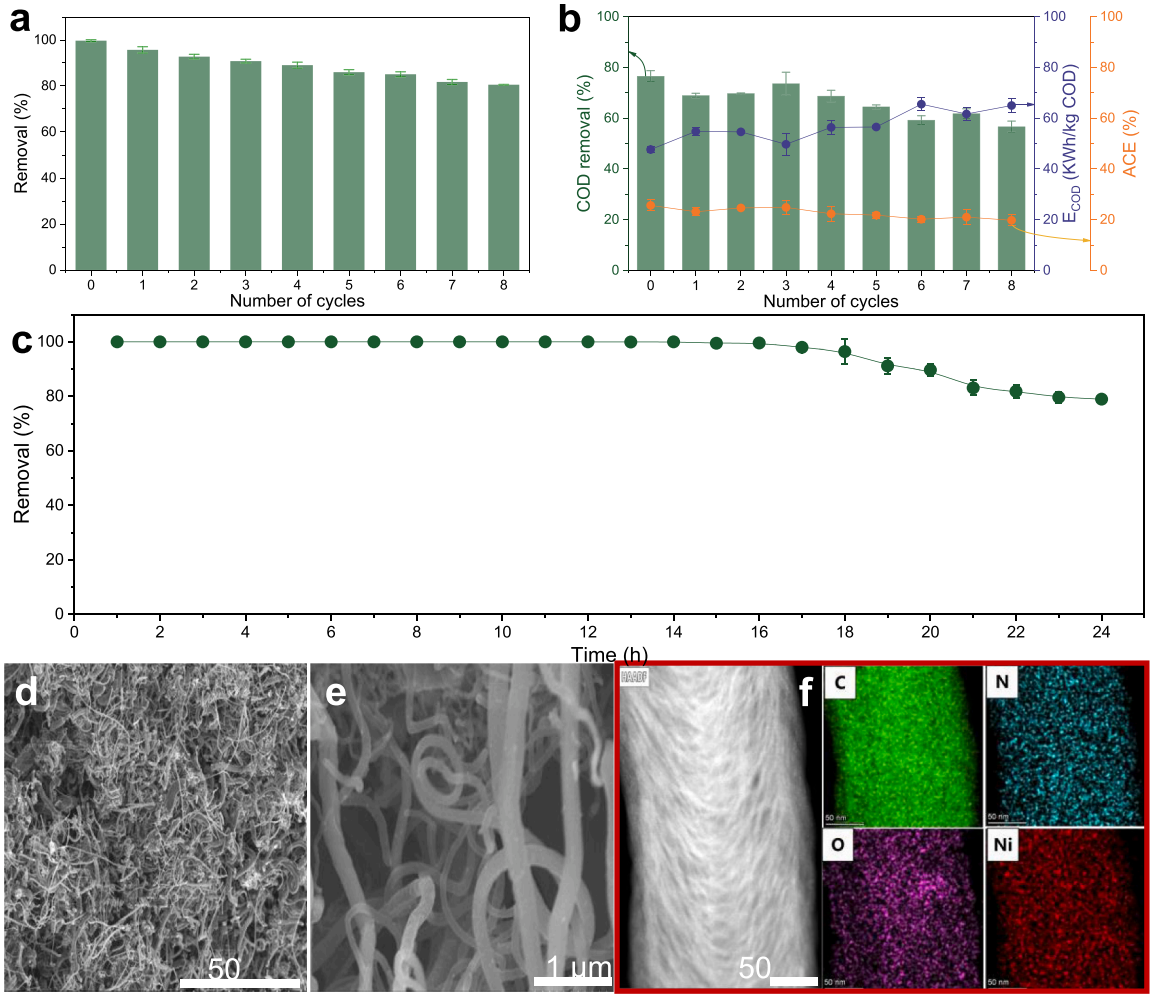

Fig. 5. (a) Cycling stability of TC removal and (b) the corresponding COD removal percentage, E_{COD} and ACE. (c) Long-term stability test during a 24-h continuous flow-through treatment. SEM images (d-e) and EDS mapping (f) of Ni-NC_{50} after the reaction.

Ni-NC_{50} were evaluated under the optimal operating conditions. As shown in Fig. 5a, during 8 consecutive cycles (totaling 16 h) of intermittent degradation, Ni-NC_{50} maintained catalytic stability. At the end of the 8th cycle, the TC removal efficiency remained at approximately 80%. Correspondingly, the COD mineralization percentage showed a gradual decrease (from initially ~78% to ~60%), while the E_{COD} slightly increased, and the ACE remained within a stable range (Fig. 5b). To simulate continuous processing conditions, a 24-h uninterrupted flow-through operation test was conducted (Fig. 5c). The results showed that during the first 17 h of continuous operation, the single-pass removal efficiency of TC by Ni-NC_{50} remained above 96%. Although the removal efficiency decreased to approximately 80% at the end of the 24-h operation, the overall performance of the system did not show a major decline, verifying the operational stability of the material in a continuous flow phase.

To analyze the mechanism behind the activity decay, the structural and interfacial chemical states of the post-reaction Ni-NC_{50} were characterized. From a morphological perspective, post-used SEM imaging revealed that after prolonged fluid flushing and electrochemical polarization, both electrodes maintained their structural integrity. Specifically, the intertwined 3D carbon nanofiber network of the spent anode (Fig. 5d) and the carbon nanotube architecture of the spent cathode (Fig. S25) exhibited no observable fiber breakage or framework collapse. However, the textural properties underwent noticeable changes. According to the N_2 adsorption-desorption measurements (Figure S25 and Figure S26), the SSA of both the anode and the cathode experienced a drastic reduction from 31.77 $m^2\ g^{-1}$ to approximately 13.85 $m^2\ g^{-1}$. This significant loss of porosity strongly implies the occurrence of internal pore blockage during continuous wastewater treatment, rather than structural destruction.

Despite the textural changes, the chemical configurations of the active sites exhibited extraordinary resilience against the hypersaline oxidative environment. Elemental mapping confirmed that the Ni active centers remained uniformly dispersed on the carbon skeleton. More importantly, comprehensive quantitative XPS analysis (Fig. S27 and Table S4–S5) explicitly ruled out metal leaching or nitrogen depletion: the total atomic percentages of Ni and N on the anode remained strictly stable (1.02 → 0.98 at. % and 7.55 → 7.69 at. %, respectively). Spectral deconvolution of the N 1s peak revealed that the proportions of all nitrogen configurations, including Pyridinic-N (0.882 → 0.897 at. %), Graphitic-N (2.153 → 2.147 at. %), Pyrrolic-N (0.769 → 0.752 at. %), and the critical covalently bound Ni-N_x motifs (3.21 → 3.32 at. %), were remarkably well-preserved. Recent milestone studies have profoundly established that conventional Ni-based precatalysts typically undergo dynamic surface reconstruction under strong anodic polarization, evolving into highly active, amorphous high-valence phases such as NiOOH [78,79]. However, the post-reaction Ni 2p deconvolution revealed that while trace amounts of metallic Ni^0 naturally oxidized (0.087 → 0.012 at.%), the high-valence Ni^{3+} states (0.357 → 0.371 at.%) and Ni^{2+} states (0.576 → 0.597 at.%) maintained a steady distribution. This confirms no massive irreversible accumulation of NiOOH phases occurred. This extraordinary structural preservation can be reconciled with the reconstruction theory through the lens of strong spatial confinement and reaction specificity. Unlike bulk metal oxides that undergo deep irreversible lattice reconstruction during oxygen evolution, the Ni sites in our system are strongly tethered within the rigid carbon lattice via covalent Ni-N bonds, which restricts destructive lattice restructuring. Furthermore, in the chloride-rich matrix (CER-dominant), the highly facile electron transfer kinetics to Cl^- allow the Ni centers to rapidly cycle. Consequently, any highly active NiOOH-like intermediates formed operando under applied potential behave as highly reversible transient species, swiftly returning to their stable Ni-N_x resting state upon the cessation of electrolysis. Ultimately, this confined, highly reversible dynamic evolution ensures exceptional long-term chemical durability.

Since the fundamental chemical structure of the Ni-N_x active sites and the carbon skeleton remained completely intact, the later-stage performance decay is explicitly ascribed to physical pore fouling, which is elegantly corroborated by the oxygen speciation data. The overall oxygen content increased on both the anode (0.92 → 1.40 at.%) and the cathode (0.92 → 1.33 at.%). For the cathode, this mild oxidation is driven by localized surface hydroxylation induced by the alkaline microenvironment of the hydrogen evolution reaction. For the anode, high-resolution O 1s deconvolution provided a definitive idea. While the structural lattice oxygen (Ni-O and C-OH) showed minimal variations, the oxygen enrichment was almost entirely driven by the massive accumulation of C═O (0.276 → 0.423 at.%) and C-O-C (0.313 → 0.567 at.%) functional groups. These specific groups are the quintessential characteristic signatures of oxygen-rich intermediate fragments derived from TC degradation. This quantitatively proves that under continuous high-concentration organic loading, recalcitrant macromolecular/oligomeric intermediates progressively accumulate and physically adsorb within the hierarchical micro/mesopores. This physical masking temporarily covers the active sites and hinders interfacial mass transfer, which accounts for the performance decline. Collectively, these characterizations verify that the Ni-NC_{50} material possesses exceptional intrinsic chemical stability.

3.6. Biological toxicity analysis

To evaluate the toxicity reduction of the electrocatalytic oxidation system on the TC wastewater, toxicological analyses were conducted using human hepatocellular carcinoma (HepG2) cell viability assays and mung bean (*Vigna radiata*) germination tests.

As shown in Fig. 6a, the electrocatalytic treatment altered the cytotoxicity of the water samples. In the CCK-8 assay, a normal culture medium was used as the negative control (NC, 100%), and a system containing an equal proportion of pure water was set as the blank control (BC, 94%) to eliminate solvent effects. The results showed that the undegraded TC solution inhibited HepG2 cell proliferation, with the cell viability decreasing to 59.75%. After the electrocatalytic treatment, the cell viability in the degraded solution increased to 84.5%. However, the cell viability of the degraded group was slightly lower than that of the BC group, suggesting the potential presence of trace residual intermediates with biological activity. This also reflected the sensitivity of mammalian cells to trace organic pollutants.

The detoxification effect of the treated system was further evaluated through phytotoxicity tests (Fig. 6b and c). The different water samples showed distinct effects on the early development of mung beans. After 6 days of exposure (Fig. 6b), the undegraded group exhibited phytotoxicity. The germination process was delayed, the final seedling fresh weight was 0.29 g, and the stem length was limited to 2.93 cm. In contrast, the morphological development and germination behavior of mung beans in the treated group were largely restored. The fresh weight (0.40 g) and stem length (7.75 cm) were comparable to those of the pure water control group (0.41 g and 7.82 cm, respectively). These results suggest that the electrocatalytic treatment effectively reduced the biological toxicity of the wastewater.

A critical challenge in chloride-mediated electrocatalytic oxidation is the potential parasitic over-oxidation of active chlorine into highly toxic and persistent inorganic oxyanions, particularly chlorate (ClO_3^-) and perchlorate (ClO_4^-). To evaluate the environmental safety of the effluent, Ion Chromatography was employed (Table S5). Remarkably, despite the high chloride background (2 wt% g/L NaCl), the concentrations of ClO_3^- and ClO_4^- in the final effluent were restricted to trace levels of merely 0.111 mg L^{-1} and 0.224 mg L^{-1}, respectively. While the system restricts oxyanion accumulation, their environmental relevance must be critically benchmarked against regulatory standards. The generated ClO_3^- level (0.111 mg/L) is well below the stringent WHO drinking water limit (0.7 mg L^{-1}). However, the trace ClO_4^- (0.224 mg L^{-1}) exceeds the strict regulatory standards for pristine water sources (e.g., 0.015 mg L^{-1} advised by US EPA). Nevertheless, the comprehensive biological

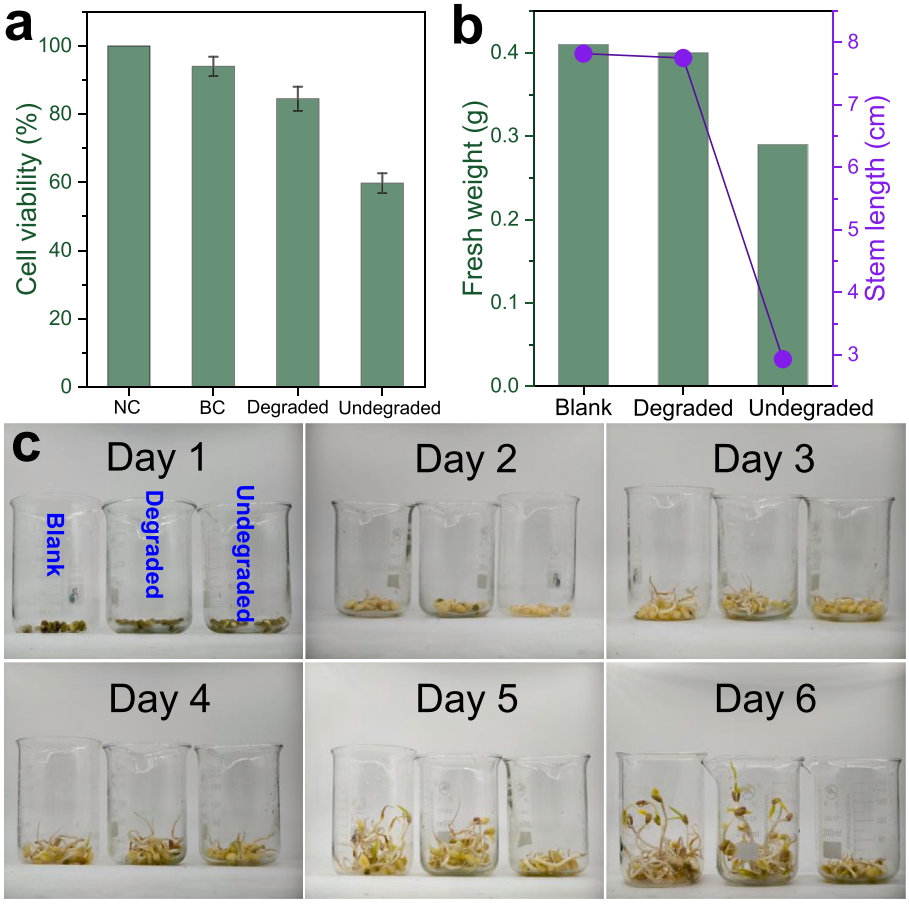

Fig. 6. Toxicity evaluation of the TC solutions before and after electrocatalytic degradation. (a) Viability of HepG2 cells exposed to the different water samples (NC: negative control; BC: blank control). (b) Fresh weight and stem length of the mung bean seedlings after exposure to the different water samples. (c) Photographs of the germination and growth of mung beans under the different treatments from day 1 to day 6.

assessments confirmed that the treated effluent successfully restored normal biological functions (Fig. 6), demonstrating a substantial net reduction in acute ecological toxicity by eradicating the primary organic hazard. Furthermore, this system is designed as a decentralized pre-treatment for hyper-concentrated industrial effluents. In practical engineering, integrating this pre-treated stream into municipal biological networks allows for massive volumetric dilution (a minimal factor of ~15 readily satisfies EPA limits) and subsequent biological reduction by anaerobic microorganisms, which safely and thoroughly mitigates the residual ClO_4^-. Nonetheless, advancing anode selectivity to suppress trace oxyanion formation at the source remains a pivotal direction for future research.

3.7. Applications

In practical medical or aquaculture wastewater, various antibiotics with complex structures often coexist in mixtures. To verify the applicability of the self-supported Ni-NC_{50} flow-through electrode in the remediation of complex water bodies, the degradation performance of the system against 9 typical antibiotics from 5 categories was evaluated. Based on the parent compound removal efficiency, COD removal percentage, and energy efficiency indicators (E_{COD} and ACE) presented in Fig. 7, the system exhibited a structure-activity relationship for substrates with different topologies.

For metronidazole (MTZ), amoxicillin (AMX), and ceftazidime (CAZ), the Ni-NC_{50} system showed COD removal percentages of 88.2%, 82.7%, and 84.1%, respectively. From the perspective of molecular topology, the core pharmacophore (β-lactam ring) of AMX and CAZ is a four-membered ring structure with spatial strain. At the electrocatalytic interface, the electrophilic FAC and •OH induced the cleavage of the amide bond in this four-membered ring. Similarly, the smaller molecular volume and electron-rich imidazole ring side chain of MTZ made it a target for electrophilic attack. After the initial ring-opening process, the intermediates were gradually converted into smaller molecules, with only a small amount of aromatic species detected. This suggests that side reactions may be relatively limited during the degradation process, which could be related to the relatively high mineralization and current efficiency (ACE of 19-25%).

For chloramphenicol (CAP) and the fluoroquinolones ciprofloxacin (CIP) and ofloxacin (OFLX), high removal efficiencies of the parent compounds (>87%) and COD removal above 70% were achieved. During the degradation of CIP and OFLX, the E_{COD} values were 38.66 and 40.49 kWh kg^{-1} COD, respectively, with corresponding ACE values of 26-28%.The molecular structures of CIP and OFLX contain electron-rich piperazine (or methylpiperazine) groups, which are likely to serve as reactive sites for electrophilic species such as FAC [80]. This feature may promote their transformation under flow-through electrocatalytic conditions. In addition, the dichloroacetamide group in CAP also appears to be susceptible to oxidative transformation, indicating that the system is effective for the degradation of halogenated antibiotics.

For TC homologs (oxytetracycline (OTC), chlortetracycline (CTC), and doxorubicin (DOX)), high parent compound conversion (93.3%-98.1%) was achieved, while the COD removal remained in the range of 62.4%-66.1%, indicating a gap between transformation and mineralization. These antibiotics share a rigid naphthacene fused-ring structure [81]. which may influence their degradation behavior. In the initial

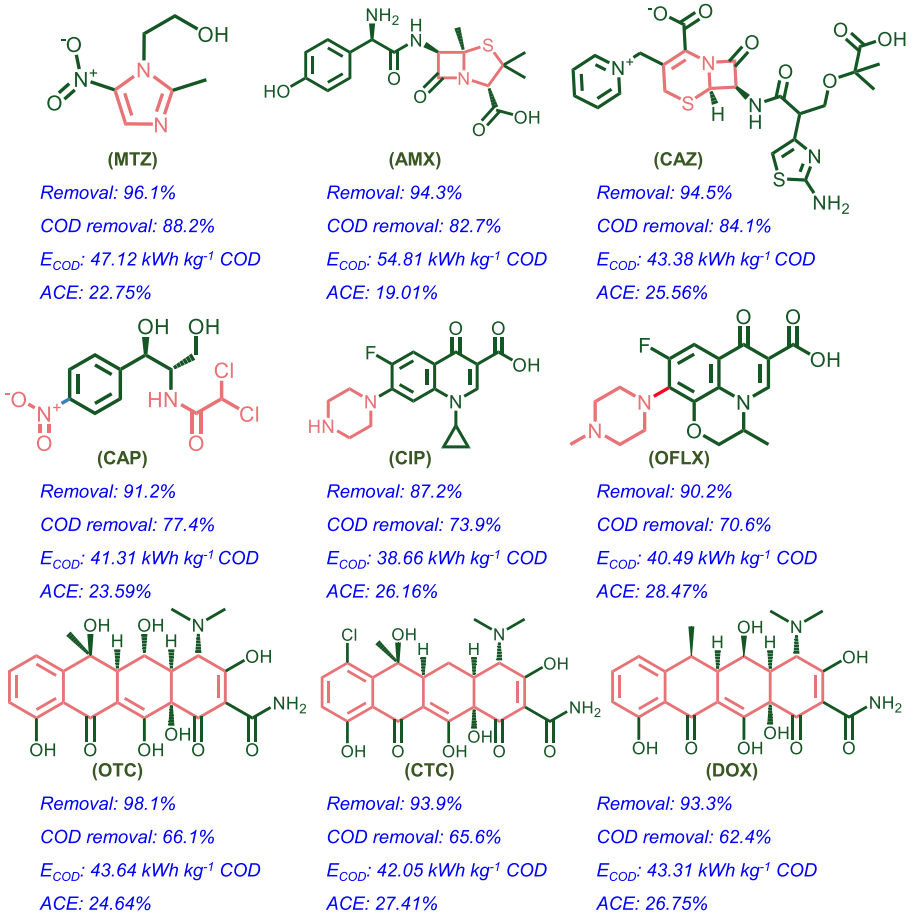

Fig. 7. Degradation performance of Ni-NC_{50} toward different antibiotics.

stage, reactive species such as FAC and •OH are likely to preferentially attack electron-rich functional groups (e.g., phenolic hydroxyl and dimethylamino groups), promoting the transformation of the parent molecules. However, the low-molecular-weight intermediates formed after ring opening may not be fully mineralized into CO_2 and H_2O within the limited hydraulic retention time, leading to relatively lower COD removal. The corresponding E_{COD} remained at 42-43 kWh kg^{-1} COD, suggesting that the system can effectively transform these compounds without a substantial increase in energy input.

Overall, the self-supported Ni-NC_{50} flow-through system likely involves a combined oxidation pathway of FAC and •OH. These reactive species may interact with different functional groups in antibiotic molecules, such as heterocyclic structures, amino side chains, and phenolic groups, contributing to their transformation. This behavior suggests that the system can be applied to antibiotics with diverse molecular structures and may have potential for the treatment of complex industrial wastewater containing mixed antibiotic contaminants.

4. Conclusion

In this study, a Ni-NC electrode with a three-dimensional hierarchical pore structure was prepared via a one-pot confined pyrolysis method, which displayed the high electrocatalytic degradation of TC in a flow-through electrocatalytic system. Under optimal parameters, the system achieved a 95.82% TC removal efficiency and 64.93% mineralization, with a low E_{COD} of 38.27 kWh kg^{-1} COD. Through structure-activity relationship and kinetic analyses, it was confirmed that the interfacial high-valence Ni^{3+} coordination structure acted as the primary active site driving the reaction, which decreased the E_a of TC electrocatalytic oxidation to 28.9 kJ mol^{-1} and accelerating the catalytic process. Meanwhile, in saline wastewater, the Ni-NC_{50} anode triggered the CER, inducing the generation of FAC as the primary species, accompanied by the chain conversion of •OH and CRs. These radicals may contribute to the transformation of electron-rich functional groups in TC molecules, accompanied by ring opening and subsequent degradation. The stability of the system was evaluated over eight consecutive cycles and a 24 h continuous operation, during which the removal efficiency was maintained within 80%-96%. In addition, the system exhibited applicability toward nine antibiotics from five structural categories, including strained rings, nitrogen-containing heterocycles, and fused-ring compounds. Toxicity assessments based on HepG2 cell viability and mung bean (*Vigna radiata*) germination further showed that the treated water samples had significantly reduced biological effects compared with the untreated solution. Overall, these results suggest that the prepared Ni-NC as electrode with the flow-through model can maintain stable performance under continuous operation and may be suitable for the treatment of complex saline wastewater containing multiple antibiotics.

CRediT authorship contribution statement

Yingjie Ruan: Validation, Methodology, Investigation, Data curation. **Jiangnan Huang:** Writing – review & editing, Resources, Methodology, Investigation. **Ruping Yan:** Investigation, Formal analysis, Data curation. **Xingan Cheng:** Resources, Methodology. **Hao-Fan Wang:** Resources, Methodology. **Hongjuan Wang:** Resources, Methodology. **Peng Zhao:** Writing – review & editing, Resources. **Hao Yu:** Resources, Methodology. **Yonghai Cao:** Writing – review & editing, Supervision, Resources, Project administration, Methodology, Funding acquisition.

Declaration of competing interest

The authors declare that they have no known competing financial interests or personal relationships that could have appeared to influence the work reported in this paper.

Acknowledgements

We would like to acknowledge the financial support from the National Natural Science Foundation of China (22272056), Guangdong Basic and Applied Basic Research Foundation (2026A1515010721), CNPC Innovation Found (2021DQ02-0704), Research Fund Program of Guangdong Provincial Key Laboratory of Fuel Cell Technology (FC202305).

Appendix A. Supplementary data

Supplementary data to this article can be found online at https://doi.org/10.1016/j.carbon.2026.122113.

References

[1] Y. Amangelsin, Y. Semenova, M. Dadar, M. Aljofan, G. Bjorklund, The impact of tetracycline pollution on the aquatic environment and removal strategies, Antibiotics (Basel) 12 (3) (2023) 440.
[2] P. Mahamallik, S. Saha, A. Pal, Tetracycline degradation in aquatic environment by highly porous MnO2 nanosheet assembly, Chem. Eng. J. 276 (2015) 155–165.
[3] A. Pena, M. Paulo, L.J.G. Silva, M. Seifrtová, C.M. Lino, P. Solich, Tetracycline antibiotics in hospital and municipal wastewaters: a pilot study in Portugal, Anal. Bioanal. Chem. 396 (8) (2010) 2929–2936.
[4] A. Chen, Y. Chen, C. Ding, H. Liang, B. Yang, Effects of tetracycline on simultaneous biological wastewater nitrogen and phosphorus removal, RSC Adv. 5 (73) (2015) 59326–59334.
[5] X. Cai, C. Liu, S. Fu, W. Shi, Z. Huang, M. Zhao, Assessing reactor configuration and bioaugmentation to enhance methane recovery from continuous anaerobic treatment of high-salinity pharmaceutical wastewater, Bioresour. Technol. 445 (2026) 134099.
[6] M. Li, X. Wang, M. Ma, J. Wu, Y. Chen, J. Ou, X. Chen, Q. Zhou, W. Sang, S. Xu, L. Cai, D. Li, Efficient treatment of high-concentration pharmaceutical wastewater with high-salinity by chemical synthesis coupling with evaporation: from lab-scale to pilot-scale, Chem. Eng. J. 496 (2024) 154278.
[7] A.J. dos Santos, H. Shen, M.R.V. Lanza, Q. Li, S. Garcia-Segura, Electrochemical oxidation of surfactants as an essential step to enable greywater reuse, Environ. Technol. Innov. 34 (2024) 103563.
[8] M.S. Gaber, S. Garcia-Segura, M.R.V. Lanza, A.J. dos Santos, Enabling decentralized treatment of BPA through electrified photo-activated advanced oxidation, Sep. Purif. Technol. 382 (2026) 136095.
[9] A.J. dos Santos, E. Brillas, A review of anodic oxidation, electro-Fenton and electrochemical nitrate reduction: a decade of advances and future directions, J. Electroanal. Chem. 1009 (2026) 119996.
[10] N. Ormeno-Cano, J. Radjenovic, Electrochemical degradation of antibiotics using flow-through graphene sponge electrodes, J. Hazard Mater. 431 (2022) 128462.
[11] J.Z. Xie, J.X. Ma, C.Y. Zhang, T.D. Waite, Direct electron transfer (DET) processes in a flow anode system-energy-efficient electrochemical oxidation of phenol, Water Res. 203 (2021) 117547.
[12] Z. Liu, H.Z. Yang, B.X. Ren, Y. Qin, Y.W. Fu, M.Y. Si, Z.Y. Li, J.H. Zhang, Y. Chen, Mass transfer in electrochemical advanced oxidation processes: a comprehensive review of characterization, influencing factors, and computational fluid dynamics simulations, J. Water Process Eng. 81 (2026) 109304.
[13] I. García-López, L.F. Arenas, T. Turek, V.I. Agueda, A. Garrido-Escudero, Mass transfer enhancement in electrochemical flow cells through 3D-printed biomimetic channels, React. Chem. Eng. 8 (7) (2023) 1776–1784.
[14] I. Hakizimana, X. Zhao, C. Wang, E. Mutabazi, C. Zhang, Insights into the flow-through electrochemical system in water and wastewater treatment: influential factors, advantages, challenges, and perspective, Sep. Purif. Technol. 331 (2024) 125533.
[15] F.C. Moreira, R.A.R. Boaventura, E. Brillas, V.J.P. Vilar, Electrochemical advanced oxidation processes: a review on their application to synthetic and real wastewaters, Appl. Catal. B Environ. Energy 202 (2017) 217–261.
[16] I. Sirés, E. Brillas, M.A. Oturan, M.A. Rodrigo, M. Panizza, Electrochemical advanced oxidation processes: today and tomorrow. A review, Environ. Sci. Pollut. Res. 21 (14) (2014) 8336–8367.
[17] T.X.H. Le, H. Haflich, A.D. Shah, B.P. Chaplin, Energy-efficient electrochemical oxidation of Perfluoroalkyl substances using a Ti4O7 reactive electrochemical membrane anode, Environ. Sci. Technol. Lett. 6 (8) (2019) 504–510.
[18] E. Garcia-Bordejé, A.M. Benito, W.K. Maser, Graphene aerogels via hydrothermal gelation of graphene oxide colloids: Fine-tuning of its porous and chemical properties and catalytic applications, Adv. Colloid Interface Sci. 292 (2021) 102420.
[19] S. Chen, K.J. Huang, H.F. Wang, H.J. Wang, H. Yu, J.N. Huang, Y.H. Cao, Electric-field enhanced three-dimensional flexible carbon felt as a host for Pt 4+ions extraction, Chem. Eng. J. 490 (2024) 151835.
[20] B. Wang, Q. Jiang, G.X. Yang, H.F. Wang, H.J. Wang, F. Peng, H. Yu, J.N. Huang, G. Y. Zhong, Y.H. Cao, Electric field-assisted uptake of hexavalent chromium ions with in situ regeneration of carbon monolith adsorbents, Adv. Sci. 10 (21) (2023) 2301419.
[21] J.N. Huang, B. Wang, H.F. Wang, H.J. Wang, H. Yu, Y.H. Cao, Synergistic decontamination of hexavalent chromium and organic pollutants via dual-functional carbon monolith: deciphering Electrosorption-Electroreduction interplay, Sep. Purif. Technol. 382 (2026) 135773.
[22] Y.A. Ji, J. Du, A.B. Chen, X.Q. Gao, M.K. Peng, Transition metal-nitrogen-carbon single-atom catalysts enhanced CO2 electroreduction reaction: a review, ChemSusChem 18 (3) (2025) 202405117.
[23] M. Humayun, M. Israr, A. Khan, M. Bououdina, State-of-the-art single-atom catalysts in electrocatalysis: from fundamentals to applications, Nano Energy 113 (2023) 108570.
[24] Y. Yang, L. Yang, Q. Zhang, Y. Li, L. Cao, Q. Li, C. Fu, C. Sheng, S. Zhang, H. Xie, P. Zhang, Fe-N4 single-atom nitrogen doped carbon catalyst: Dual-functional design for PMS-activated antibiotic degradation and efficient oxygen reduction reaction, Chem. Eng. J. 527 (2026) 171819.
[25] S. Patar, R. Mittal, F. Yasmin, B.K. Bhuyan, L.J. Borthakur, Photocatalytic degradation of antibiotics by N-doped carbon nanoflakes-nickel ferrite composite derived from algal biomass, Chemosphere 363 (2024) 142908.
[26] J. Yang, P. Li, X. Duan, D. Zeng, Z. Ma, S. An, L. Dong, W. Cen, Y. He, Insights into the role of dual reaction sites for single Ni atom Fenton-like catalyst towards degradation of various organic contaminants, J. Hazard Mater. 430 (2022) 128463.
[27] H. Cui, J. Zhang, C. Chen, Designing single-atom catalysts: bridging metal-support interaction and adsorption energy optimization, Chem. Sci. 17 (4) (2026) 2001–2027.
[28] M. Hu, D. Zhao, X. Yan, Y. Wang, J. Zhang, X. Hu, M. Zhou, P. Liu, Enhanced peroxymonosulfate activation for antibiotic and heavy metal removal using ZIF-67-derived magnetic Ni/Co-LDH@NC: bimetallic electronic synergy and oxygen vacancy effects, Appl. Catal. B Environ. Energy 362 (2025) 124753.
[29] F.-H. Hu, Q.-F. Ye, S.-R. Chen, Y.-W. Yu, H. Chen, S.-F. Qin, L.-X. You, X.-C. Tian, F. Zhao, Electrocatalytic synergistic degradation of tetracycline by low-energy-consumption Mn0.22-NiS nanosheet electrodes: interface mechanism and toxicity analysis, Chem. Eng. J. 519 (2025) 165514.
[30] D. Li, Y. Zhao, J. Zhang, Y. Wang, D. Ghani, X. Yang, B. Zeng, I.Y. Zhang, R. Huang, Electrocatalytic degradation of naphthenic acids using reduced graphene oxide modified nickel foam cathode: role of surface structure and superoxide radical, Chem. Eng. J. 500 (2024) 156699.
[31] M. Wang, Y. Tang, J. Wang, Z. Xu, Q. Dong, T. Ma, B. Lai, Promoted peroxydisulfate activation by nitrogen-doped carbon embedding iron on a nickel foam cathode: performance, mechanism and relationship between CO and 1O2 generation, Chem. Eng. J. 460 (2023) 141638.
[32] J. Kim, T. Lim, D. Hernández-Castillo, J.S. Lim, J. Park, D. Kim, J. Kim, J. Ryu, Y. J. Sa, J.H. Lee, Y.J. Hwang, H.R. Moon, K.S. Exner, S.H. Joo, Identification of Ni-N4 active sites in atomically dispersed Ni catalysts for efficient chlorine evolution reaction, J. Am. Chem. Soc. 147 (31) (2025) 27664–27675.
[33] N.N. Cai, L.J. Fu, Z.X. Yang, D.K. Huang, Innovative strategies to effectively increase the active- site density of M-N-C materials for electrochemical application, Curr. Opin. Electrochem. 34 (2022) 100994.
[34] X.X. Wang, X.H. Wu, W. Ma, X.C. Zhou, S. Zhang, D.H. Huang, L.R. Winter, J. H. Kim, M. Elimelech, Free-standing membrane incorporating single-atom catalysts for ultrafast electroreduction of low-concentration nitrate, Proc. Natl. Acad. Sci. 120 (11) (2023) 703120.
[35] K. Kumar, L. Dubau, F. Jaouen, F. Maillard, Review on the degradation mechanisms of Metal-N-C catalysts for the oxygen reduction reaction in acid electrolyte: current understanding and mitigation approaches, Chem. Rev. 123 (15) (2023) 9265–9326.
[36] Q.Q. Pang, X.Z. Fan, K.H. Sun, K. Xiang, B.J. Li, S.F. Zhao, Y.D. Kim, Q.Y. Liu, Z. Y. Liu, Z.K. Peng, Nickel-Nitrogen-Carbon (Ni-N-C) electrocatalysts toward CO2 electroreduction to CO: Advances, optimizations, challenges, and prospects, Energy Environ. Mater. 7 (5) (2024) 12731.
[37] J. Tong, W. Xu, S. Bai, X. Zhao, J. Qian, "P-Strengthening Strategy" of nickel single-atom catalyst with boosting selective generation of nonradicals: synergy of metal Center and substrate, Adv. Funct. Mater. 35 (47) (2025) 2508487.
[38] H. Zhang, T.Y. Tang, H.F. Wang, H.J. Wang, Y.H. Cao, H. Yu, Topological conversion of nickel foams to monolithic single-atom catalysts, Adv. Funct. Mater. 34 (16) (2024) 2312939.
[39] Y. Qiu, H.B. Yang, L. Ma, Y. Lin, H.W. Zong, B. Wen, X.Y. Bai, M.Q. Wang, In situ-derived carbon nanotube-decorated nitrogen-doped carbon-coated nickel hybrids from MOF/melamine for efficient electromagnetic wave absorption, J. Colloid Interface Sci. 581 (2021) 783–793.
[40] B. Li, Z. Wang, F. Nie, M. Zhang, H. Zhang, Synergistic promotion by Ni single atoms and Ni nanoclusters for efficient electrocatalytic oxidation of ammonia, Sep. Purif. Technol. 374 (2025) 133681.
[41] D.W. Liu, L. Yang, F.Y. Wang, H. Zhang, J. Liu, T. Lv, H.J. Zhao, Y.C. Du, Hierarchical carbon nanotubes@Ni/C foams for high-performance microwave absorption, Carbon 196 (2022) 867–876.
[42] X.L. Li, X.T. Chen, Y.Y. Yan, F. Wang, L.Y. Feng, Y.G. Chen, Nitrogen-doped graphene for tetracycline removal via enhancing adsorption and non-radical persulfate activation, Environ. Res. 235 (2023) 116642.

[43] K.F. Wang, C.Y. Guo, J. Li, Y.B. Wang, Y.G. Xing, P.Z. Li, Z.Y. Wang, J.D. Wang, Efficient degradation of tetracycline via N-doped carbon derived from discarded PET plastics by boosting peroxymonosulfate activation and singlet oxygen generation, Chem. Eng. J. 507 (2025) 160653.
[44] P.C.M. Laan, F.J. de Zwart, E.M. Wilson, A. Troglia, O.C.M. Lugier, N.J. Geels, R. Bliem, J.N.H. Reek, B. de Bruin, G. Rothenberg, N. Yan, Understanding the oxidative properties of nickel oxyhydroxide in alcohol oxidation reactions, ACS Catal. 13 (13) (2023) 8467–8476.
[45] L. Ma, M.H. Zhou, G.B. Ren, W.L. Yang, L. Liang, A highly energy-efficient flow-through electro-Fenton process for organic pollutants degradation, Electrochim. Acta 200 (2016) 222–230.
[46] X.T. Xu, X.L. Zeng, C.K. Zhang, R.L. Huang, W.C. Ding, Enhanced electrocatalytic removal of tetracycline using dual carbon material combined particle electrodes in a three-dimensional electrochemical system: degradation pathway and mechanism, J. Clean. Prod. 419 (2023) 138257.
[47] Y.Q. Zhang, S.J. Zuo, M.H. Zhou, L. Liang, G.B. Ren, Removal of tetracycline by coupling of flow-through electro-Fenton and in-situ regenerative active carbon felt adsorption, Chem. Eng. J. 335 (2018) 685–692.
[48] C. He, X.J. Ma, H.J. Feng, Y.C. Ding, Y.J. Xia, Z.W. Wang, Electro-activation of peroxymonosulfate using a carbon fiber membrane anode for high-efficient degradation of antibiotic wastewater: the dominant role of singlet oxygen, Chem. Eng. J. 486 (2024) 150239.
[49] M.Q. Shi, H.F. Wang, P.Q. Yuan, X.R. Xu, J.Y. Yang, Degradation of tetracycline hydrochloride by electrocatalytic oxidation using NiO@Co3O4/Tielectrode, J. Water Process Eng. 61 (2024) 105242.
[50] M.X. Ru, K. Lang, X.D. Xiao, H. Wang, H.Y. Meng, B.J. Jiang, Efficient electrocatalytic degradation of tetracycline using NiCo2O4/MnO2composite electrode: synergistic enhancement mechanisms and environmental toxicity assessment, J. Environ. Chem. Eng. 13 (2) (2025) 115947.
[51] J. Zhang, X. Tang, Y. Hong, G. Chen, Y. Chen, L. Zhang, W. Gao, Y. Zhou, B. Sun, Carbon-based single-atom catalysts in advanced oxidation reactions for water remediation: from materials to reaction pathways, Eco-Environ. Health 2 (2) (2023) 47–60.
[52] W.J. Zhang, T.T. Le, D. Shin, S. Nandy, J.W. Choi, S.Y. Paek, C.K. Hwang, J.H. Kim, H. Suh, K.H. Chae, S.Y. Lee, S.S. Han, S.H. Kim, J.M. Kim, Higher-valent nickel oxides with enhanced two-electron oxygen reduction in advanced electro-Fenton system for organic pollutants degradation, Appl. Catal. B Environ. Energy 361 (2025) 124666.
[53] X. Li, L. Liu, X. Ren, J. Gao, Y. Huang, B. Liu, Microenvironment modulation of single-atom catalysts and their roles in electrochemical energy conversion, Sci. Adv. 6 (39) (2020) eabb6833.
[54] X. Li, L. Liu, F. Yang, CFC/PVDF/GO-Fe3+ membrane electrode and flow-through system improved E-Fenton performance with a low dosage of aqueous iron, Sep. Purif. Technol. 193 (2018) 220–231.
[55] L. He, Y. Ji, J. Cheng, C. Wang, L. Jiang, X. Chen, H. Li, S. Ke, J. Wang, Effect of pH and Cl-concentration on the electrochemical oxidation of pyridine in low-salinity reverse osmosis concentrate: kinetics, mechanism, and toxicity assessment, Chem. Eng. J. 449 (2022) 137669.
[56] D.C. De Moura, C.K.C. De Araújo, C.L. Zanta, R. Salazar, C.A. Martínez-Huitle, Active chlorine species electrogenerated on Ti/Ru0. 3Ti0. 7O2 surface: electrochemical behavior, concentration determination and their application, J. Electroanal. Chem. 731 (2014) 145–152.
[57] Y. Zhang, H. Wang, Y. Li, B. Wang, J. Huang, S. Deng, G. Yu, Y. Wang, Removal of micropollutants by an electrochemically driven UV/chlorine process for decentralized water treatment, Water Res. 183 (2020) 116115.
[58] D. Chang, Y. Mao, W. Qiu, Y. Wu, B. Cai, The source and distribution of tetracycline antibiotics in China: a review, Toxics (2023) 214.
[59] Y. Yang, J. Shin, J.T. Jasper, M.R. Hoffmann, Multilayer heterojunction anodes for saline wastewater treatment: design strategies and reactive species generation mechanisms, Environ. Sci. Technol. 51 (8) (2017), 4733-4733.
[60] Z.L. Zhang, J.H. Lin, J.W. Liu, L. Li, W. Zhuang, Q.Y. Jiang, J. Liu, L. Ding, J. Shi, H. P. Deng, Effect of Cl on activated peroxymonosulfate based advanced oxidation process: transformation of radicals and mechanism of singlet oxygen generation, Sep. Purif. Technol. 367 (2025) 132821.
[61] C. Yang, Y. Fan, S.S. Shang, P. Li, X.Y. Li, Fabrication of a permeable SnO2-Sb reactive anodic filter for high-efficiency electrochemical oxidation of antibiotics in wastewater, Environ. Int. 157 (2021) 106827.
[62] S. Lu, X.C. Li, G. Zhang, S.B. Wang, Unlocking single-atom induced electronic metal-support interactions in electrocatalytic one-electron water oxidation for wastewater purification, Nat. Commun. 16 (1) (2025) 4346.
[63] J.-H. Wu, H.-Q. Yu, How do metal oxides mislead spin-trapping electron paramagnetic resonance analysis? Environ. Sci. Technol. Lett. 11 (4) (2024) 370–375.
[64] J. Cai, M. Zhou, Y. Pan, X. Du, X. Lu, Extremely efficient electrochemical degradation of organic pollutants with co-generation of hydroxyl and sulfate radicals on Blue-TiO2 nanotubes anode, Appl. Catal., B 257 (2019) 117902.
[65] Z. Zhuang, S.A. Giles, J. Zheng, G.R. Jenness, S. Caratzoulas, D.G. Vlachos, Y. Yan, Nickel supported on nitrogen-doped carbon nanotubes as hydrogen oxidation reaction catalyst in alkaline electrolyte, Nat. Commun. 7 (1) (2016) 10141.
[66] Q. Huang, Y.W. Xu, Y.Y. Guo, L.J. Zhang, Y. Hu, J.J. Qian, S.M. Huang, Highly graphitized N-doped carbon nanosheets from 2-dimensional coordination polymers for efficient metal-air batteries, Carbon 188 (2022) 135–145.
[67] C. Qiu, L. Jiang, Y. Gao, L. Sheng, Effects of oxygen-containing functional groups on carbon materials in supercapacitors: a review, Mater. Des. 230 (2023) 111952.
[68] G. Franklin, E.-M. Halim, C. Merlet, P.-L. Taberna, P. Simon, Insights into the effect of oxygen functional groups on the heterogeneous electron transfer at activated carbons from scanning electrochemical microscopy, Electrochim. Acta 465 (2023) 142944.
[69] H. Sun, S. Song, Nickel hydroxide-based electrocatalysts for promising electrochemical oxidation reactions: beyond water oxidation, Small 20 (33) (2024) 2401343.
[70] Y. Shi, Z.R. Ma, Y.Y. Xiao, Y.C. Yin, W.M. Huang, Z.C. Huang, Y.Z. Zheng, F.Y. Mu, R. Huang, G.Y. Shi, Y.Y. Sun, X.H. Xia, W. Chen, Electronic metal-support interaction modulates single-atom platinum catalysis for hydrogen evolution reaction, Nat. Commun. 12 (1) (2021) 3021.
[71] Y. Hou, M. Qiu, M.G. Kim, P. Liu, G.T. Nam, T. Zhang, X.D. Zhuang, B. Yang, J. Cho, M.W. Chen, C. Yuan, L.C. Lei, X.L. Feng, Atomically dispersed nickel-nitrogen-sulfur species anchored on porous carbon nanosheets for efficient water oxidation, Nat. Commun. 10 (2019) 1392.
[72] Y.H. Duan, D.H. Chen, R.Y. Zhang, Y.M. Du, L. Wang, Optimizing the coordination environment of active sites to enhance heterogeneous electrocatalytic performances, Coord. Chem. Rev. 522 (2025) 216243.
[73] W.K. Lai, X. Yang, Z.C. Hua, A.N. Wang, D.Q. He, Z.P. Wei, M. Yang, J.Y. Fang, Differentiating reactive chlorine species for micropollutant abatement in chloride containing water by electrochemical oxidation process, Water Res. 271 (2025) 122984.
[74] P. Wang, Y.L. He, C.H. Huang, Reactions of tetracycline antibiotics with chlorine dioxide and free chlorine, Water Res. 45 (4) (2011) 1838–1846.
[75] M.A. Oturan, M. Pimentel, N. Oturan, I. Sirés, Reaction sequence for the mineralization of the short-chain carboxylic acids usually formed upon cleavage of aromatics during electrochemical Fenton treatment, Electrochim. Acta 54 (2) (2008) 173–182.
[76] M.L. Wu, S. Zhou, X.M. Huang, Z.Q. Chen, D. Zhi, Insight into the coupled processes of electro-oxidation and other techniques for organic removal from water and wastewater, Desalination Water Treat. 324 (2025) 101458.
[77] J. Teng, S.J. You, F. Ma, X.D. Chen, N.Q. Ren, Enhanced electrochemical decontamination and water permeation of titanium suboxide reactive electrochemical membrane based on sonoelectrochemistry, Ultrason. Sonochem. 69 (2020) 105248.
[78] L. Gao, X. Cui, C.D. Sewell, J. Li, Z. Lin, Recent advances in activating surface reconstruction for the high-efficiency oxygen evolution reaction, Chem. Soc. Rev. 50 (15) (2021) 8428–8469.
[79] R. Jiang, J. Zhang, J. Gao, Y. Xie, L. Wu, Y. Wang, Z. Xu, Z.-S. Wu, S. Yuan, G. Xu, Redox promoted rapid and deep reconstruction of defect-rich nickel precatalysts for efficient water oxidation, Small 20 (43) (2024) 2401384.
[80] Q. Yang, Y. Gao, J. Ke, P.L. Show, Y. Ge, Y. Liu, R. Guo, J. Chen, Antibiotics: an overview on the environmental occurrence, toxicity, degradation, and removal methods, Bioengineered 12 (1) (2021) 7376–7416.
[81] J.R. Li, X.T. Liang, W.J. Zhou, B.Y. Liu, Z.L. Yang, Q. Yang, Nitrogen-doped iron-manganese porous carbon particle electrodes for electrocatalytic degradation of tetracycline: interfacial reaction mechanisms, Sep. Purif. Technol. 354 (2025) 129382.